Geophysical Journal International

A Bayesian Method to Quantify Azimuthal Anisotropy Model Uncertainties: Application to Global Azimuthal Anisotropy in the Upper Mantle and Transition Zone

Journal:	*Geophysical Journal International*
Manuscript ID	Draft
Manuscript Type:	Research Paper
Date Submitted by the Author:	n/a
Complete List of Authors:	Yuan, Kaiqing; University of California, Los Angeles, Earth, Planetary, and Space Sciences Beghein, Caroline; University of California, Los Angeles, Earth, Planetary, and Space Sciences
Keywords:	Seismic anisotropy < SEISMOLOGY, Seismic tomography < SEISMOLOGY, Inverse theory < GEOPHYSICAL METHODS, Probability distributions < GEOPHYSICAL METHODS, Statistical seismology < SEISMOLOGY, Surface waves and free oscillations < SEISMOLOGY

submitted to *Geophys. J. Int.*

A Bayesian Method to Quantify Azimuthal Anisotropy Model Uncertainties: Application to Global Azimuthal Anisotropy in the Upper Mantle and Transition Zone

K. Yuan[2] and C. Beghein[1]

[1] *Department of Earth, Planetary, and Space Sciences, University of California Los Angeles, Los Angeles, CA* 90095*, USA*

[2] *formerly at Department of Earth, Planetary, and Space Sciences, University of California Los Angeles, Los Angeles, CA* 90095*, USA*

SUMMARY

Seismic anisotropy is a powerful tool to constrain mantle deformation, but its existence in the deep upper mantle and topmost lower mantle is still uncertain. Recent results from higher mode Rayleigh waves have, however, revealed the presence of 1 % azimuthal anisotropy between 300 km and 800 km depth, and changes in azimuthal anisotropy across the mantle transition zone boundaries. This has important consequences for our understanding of mantle convection patterns and deformation of deep mantle material. Here, we propose a Bayesian method to model depth variations in azimuthal anisotropy and to obtain quantitative uncertainties on the fast seismic direction and anisotropy amplitude from phase velocity dispersion maps. We applied this new method to existing global fundamental and higher mode Rayleigh wave phase velocity maps to assess the likelihood of azimuthal anisotropy in the deep upper mantle and to determine whether previously detected changes in anisotropy at the transition zone boundaries are robustly constrained by those data. Our results confirm that deep upper mantle azimuthal anisotropy is favored

and well-constrained by the higher mode data employed. The fast seismic directions are in agreement with our previously published model. The data favor a model characterized, on average, by changes in azimuthal anisotropy at the top and bottom of the transition zone. However, this change in fast axes is not a global feature as there are regions of the model where the azimuthal anisotropy direction is unlikely to change across depths in the deep upper mantle. We were, however, unable to detect any clear pattern or connection with surface tectonics. Future studies will be needed to further improve the lateral resolution of this type of model at transition zone depths.

Key words: Seismic anisotropy – Tomography – Inverse theory – Probability distributions – Statistical seismology – Surface waves and free oscillations.

1 INTRODUCTION

The directional dependence of seismic wave velocity, or seismic anisotropy, is a powerful tool to investigate mantle deformation and geodynamics (Montagner 1994; Karato 1998; Becker et al. 2003; Long 2013). The lattice preferred orientation (LPO) of the crystallographic axes of elastically anisotropic material is generally assumed to be the cause of the seismic anisotropy detected in Earth's mantle, though it could alternatively be caused by the shape preferred orientation (SPO) of isotropic structures with contrasting elastic properties such as cracks, layered structures, melt tubules, or lenses (Kendall & Silver 1996; Montagner 1994). In the mantle lithosphere, frozen-in seismic anisotropy is often attributed to olivine LPO related to past tectonic processes (Karato 1989; Nicolas & Christensen 1987; Silver 1996). In the asthenosphere, olivine LPO associated with present-day mantle deformation is often invoked to explain observations of seismic anisotropy because the fast seismic direction generally aligns with the absolute plate motion (Nishimura & Forsyth 1988; Smith et al. 2004; Debayle et al. 2005; Marone & Romanowicz 2007; Beghein et al. 2014), and the preferred alignment of olivine can be used to determine the direction of mantle flow (Becker et al. 2003). In the lowermost mantle, both SPO through horizontal layering or aligned inclusions (Kendall & Silver 1996) and LPO of the post-perovskite phase (Oganov 2005) have been proposed to explain observations of anisotropy.

Most tomographic models of seismic anisotropy are obtained by regularized inversion of seismic data such as surface waves, free oscillations, and/or long-period body waves, and they all provide ample evidence for the presence of seismic anisotropy in the uppermost 250 km of the mantle. Radial anisotropy, which quantifies differences in seismic wave velocity between the vertical and horizontal directions, is required in the uppermost mantle to simultaneously explain Love and Rayleigh wave

dispersion data. It is included in the top 220 km of the one-dimensional (1-D) Preliminary Reference Earth Model (PREM) of Dziewonski & Anderson (1981), and in several 3-D radially anisotropic global models of the uppermost mantle models (see Chang et al. (2014) for a recent review). Azimuthal anisotropy, i.e. the dependence of seismic wave velocities with the azimuth of propagation, is also present in the uppermost mantle at the global scale (Montagner & Tanimoto 1991; Trampert & Woodhouse 2003; Debayle et al. 2005; Ekström 2011; Debayle & Ricard 2013; Yuan & Beghein 2013; Becker et al. 2014; Yuan & Beghein 2014; Schaeffer et al. 2016). Most global models of azimuthal anisotropy display common features at these depths, such as the alignment of the fast axes with the plate motion direction at asthenospheric depths beneath ocean basins and with the paleospreading directions in the oceanic lithosphere. 1-D models of radial anisotropy generally agree with one another, but there are discrepancies in models of lateral variations in radial anisotropy even at shallow depths (Chang et al. 2014).

The D'' layer is also known to be radially anisotropic: at the regional scale, radial anisotropy has been observed with shear-wave splitting measurements (Kendall & Silver 1996), and azimuthal anisotropy has been detected with S and Sdiff waveform modeling (Maupin et al. 2005). A few global tomographic models suggest D'' radial anisotropy is present at the global scale as well, though the effect of the crustal correction (Panning et al. 2010), of prior scaling relationships between elastic parameters (Beghein & Trampert 2004a; Beghein & Trampert 2004b; Beghein et al. 2006; Beghein 2010), and trade-offs between isotropic and anisotropic structure (Kustowski et al. 2008; Chang et al. 2014) cast doubt on the global nature of radial anisotropy at these depths. To date, there is no global azimuthal anisotropy model of the lowermost mantle.

For years, the lack of evidence for seismic anisotropy below $\sim$250 km depth was interpreted as the result of deformation by diffusion creep (Karato et al. 1995). Evidence for radial anisotropy in the deep upper mantle and uppermost lower mantle has, however, been accumulating over the past two decades. The first global model displaying radial anisotropy in the deep upper mantle was the 1-D model of Montagner and Kennett (1996), which was followed by multiple 1-D and 3-D global radial anisotropy models (Beghein & Trampert 2004b; Panning & Romanowicz 2004; Beghein et al. 2006; Panning & Romanowicz 2006; Kustowski et al. 2008; Visser et al. 2008a; Panning et al. 2010; Romanowicz & Lekić 2011; Auer et al. 2014; Chang et al. 2014; French & Romanowicz 2014; Moulik & Ekström 2014). Shear-wave splitting studies have also suggested the presence of radial anisotropy near subduction zone in the mantle transition zone (MTZ) and top of the lower mantle (Fouch & Fischer 1996; Wookey & Barruol 2002; Chen & Brudzinski 2003; Foley & Long 2011; Lynner 2015; Nowacki et al. 2015). Azimuthal anisotropy may additionally be present at these depths. It has been shown to be compatible with higher mode Love waves (Trampert & van Heijst 2002) and coupled free

oscillation data (Beghein et al. 2008; Hu et al. 2012). A study combining data from surface waves and shear-wave splitting beneath North America also suggested that azimuthal anisotropy is needed at greater depths than commonly assumed (Marone & Romanowicz 2007), and similar conclusions were drawn by Kosarian et al. (2011) for California. At the global scale, while early 3-D models did not show any significant azimuthal anisotropy below 250 km depth (Montagner & Tanimoto 1991; Debayle et al. 2005), more recent studies present about 1 % anisotropy in the deep upper mantle at least down to 400 km (Debayle & Ricard 2013; Yuan & Beghein 2013; Yuan & Beghein 2014; Schaeffer et al. 2016), and possibly even deeper down to the bottom of the MTZ and top of the lower mantle (Yuan & Beghein (2013; 2014)). There are still large discrepancies among models, but the increasing evidence for seismic anisotropy in the deep upper mantle challenges our understanding of mantle deformation (Figure 1).

Our previously published global azimuthal anisotropy model (Yuan & Beghein 2013), hereafter referred to as YB13SVani, not only displayed a non-negligible amount of azimuthal anisotropy (1 to 3 %) below 250 km depth, but it also revealed changes in the seismic fast direction at the MTZ boundaries. The interpretation of these results is non-unique due to the paucity of mineral physics data on MTZ material anisotropy. Nevertheless, they have important consequences for our understanding of mantle convection and the anisotropy of deep upper mantle material as it could imply changes in mantle flow direction at the MTZ, changes in volatile content, in slip system in MTZ material, etc. It is thus essential to determine which model features are robust.

In this paper, we present a Bayesian forward modeling method to quantify uncertainties and trade-offs of azimuthal anisotropy model parameters. Like most tomographic models, YB13SVani was obtained by regularized inversion of seismic data. In this particular case, the model was derived from fundamental and higher mode surface wave phase velocity maps. Estimating reliable model uncertainties from linear inversions is, however, not straightforward since most inversions yield a posterior model covariance smaller or equal to the prior covariance by construction (Tarantola 1987). If there is a large model null-space, the posterior covariance can be strongly underestimated (Trampert 1998), making both the interpretation and the uncertainty assessment of tomographic models difficult (Beghein & Trampert 2003; Beghein 2010). Model space search approaches are generally better suited to determine posterior model uncertainties as they can explore a larger part of the model space, including the null-space, and map the range of models that can fit the data reasonably well. In some cases, this type of method can even find solutions to the problem that could not be found with traditional inverse methods (Beghein & Trampert 2003). In this paper, we modeled azimuthal anisotropy in the upper mantle and topmost lower mantle and quantified parameter uncertainties and trade-offs using the Neighbourhood Algorithm (Sambridge 1999a; Sambridge 1999b), hereafter referred to as the NA.

Among many other applications, this direct search technique has been used successfully to model inner core anisotropy (Beghein & Trampert 2003), regional and global mantle seismic velocities (Beghein et al. 2002; Snoke & Sambridge 2002), and radial anisotropy (Beghein & Trampert 2004a; Beghein & Trampert 2004b; Beghein et al. 2006; Visser et al. 2008a; Yao et al. 2008; Beghein 2010). Yao (2015) recently proposed a two-step method using the NA to model azimuthal anisotropy from fundamental mode surface waves. However, as explained in section 3, the author did not display or discuss the posterior uncertainties on the fast seismic direction and the anisotropy amplitude. The method we present here solves the linear problem that relates azimuthal anisotropy elastic parameters to phase velocities using laterally varying sensitivity kernels to account for variations in crustal structure, and quantifies model uncertainties for the azimuthal anisotropy amplitude and the fast axes directions.

2 PHASE VELOCITY DATA

2.1 Phase Velocity Anisotropy

In this study, we employed the same dataset as we did to construct YB13SVani (Yuan & Beghein 2013). It consists in the fundamental and first six higher mode anisotropic Rayleigh wave phase velocity maps determined by Visser et al. (2008b). There were 16 fundamental modes between 35 s and 175 s, 16 first overtones between 35 s and 172 s, 15 second overtones between 35 s and 150 s, 11 third overtones between 35 s and 88 s, 8 fourth overtones between 35 s and 62 s, 7 fifth overtones between 35 s and 56 s, and 6 sixth overtones between 35 s and 51 s. This type of seismic data is ideal to provide depth constraints on Earth's internal structure because of their dispersive properties (Figure 2). In addition, combining fundamental and higher mode surface wave data significantly increases the depth resolution of tomographic models. Contrary to fundamental mode surface waves, which can only resolve the top $\sim$200-300 km of the mantle, the set of higher modes employed here have sensitivity to azimuthal anisotropy well into the deep upper mantle and topmost lower mantle (Figure 3).

At any given point at Earth's surface, perturbations dc in surface wave phase velocity with respect to predictions from a reference Earth model can be expressed as a function of the azimuth of propagation Ψ as follows (Montagner & Nataf 1986):

$$\begin{aligned} dc(T,\Psi) = dc_0(T) &+ dc_1(T)cos(2\Psi) + dc_2(T)sin(2\Psi) \\ &+ dc_3(T)cos(4\Psi) + dc_4(T)sin(4\Psi) \end{aligned} \quad (1)$$

where T is the period of the wave. dc_0 represents the phase velocity anomaly averaged over all azimuths and the dc_i ($i = 1, , 4$) terms represent the azimuthal dependence of the phase velocity. The 2Ψ terms can help constrain depth variations in vertically polarized shear (SV) wave azimuthal anisotropy,

and the 4Ψ terms can help determine horizontally polarized shear (SH) wave anisotropy. Equation 1 is valid for fundamental and higher mode surface waves.

The relation between 2Ψ phase velocity anisotropy and azimuthal anisotropy at depth is given by the following set of equations (Montagner & Nataf 1986):

$$dc_1(T) = \int [G_c(r)K_G(T,r) + B_c(r)K_B(T,r) + H_c(r)K_H(T,r)]\, dr \quad (2)$$

$$dc_2(T) = \int [G_s(r)K_G(T,r) + B_s(r)K_B(T,r) + H_s(r)K_H(T,r)]\, dr \quad (3)$$

where elastic parameters $G_c(r)$ and $G_s(r)$ relate to V_{SV} azimuthal anisotropy, and $B_c(r)$ and $B_s(r)$ relate to P-wave azimuthal anisotropy. $H_s(r)$ and $H_c(r)$ do not control body wave azimuthal anisotropy and only appear in surface waves (Montagner & Nataf 1986) and in normal modes (Beghein et al. 2008). $K_G(r,T)$, $K_B(r,T)$, and $K_H(r,T)$ are the local partial derivatives, or sensitivity kernels, for Rayleigh wave at period T and radius r, which can be calculated for a reference model using normal mode theory (Takeuchi 1972). The fast azimuth of propagation Θ and the anisotropy amplitude G of vertically polarized shear-waves are given by:

$$\Theta = \frac{1}{2}\arctan(G_s/G_c) \quad (4)$$

and

$$G = \sqrt{G_s^2 + G_c^2} \quad (5)$$

Similar relations exist for $B_{c,s}$ and $H_{c,s}$. Examples of kernels calculated using model PREM (Dziewonski & Anderson 1981) are shown in Figures 2 and 3, and demonstrate that including higher modes in the dataset significantly increases and extends the sensitivity to anisotropy into the deep upper mantle.

Fundamental mode Rayleigh waves typically are not expected to have a strong 4Ψ dependence in comparison to the 2Ψ terms, as demonstrated by Montagner & Tanimoto (1991) for realistic petrological models. The same may not, however, be true for higher modes since they are sensitive to deeper structure (Figure 3), and indeed Visser et al. (2008b) determined that a 4Ψ dependence significantly improved the fit of their Rayleigh wave fundamental and higher mode phase velocity path-averaged measurements (Visser et al. 2008b). Nevertheless, because the sensitivity of fundamental and higher mode Rayleigh waves to SH anisotropy is very small, here we only used the 2Ψ terms of equation 1 to build a 3-D model of SV azimuthal anisotropy in the top 1000 km of the mantle.

2.2 Phase Velocity Resolution

As explained by Visser et al. (2008b), the lateral resolution of their phase velocity models generally decreases with increasing overtone number because the quality of the path azimuthal coverage (and thus the number of modes measured reliably) decreases with the overtone number. Ray coverage was

very good everywhere for the fundamental modes, and in most continental regions and the northwestern Pacific for the higher modes, but it was poorer for the third through sixth higher modes in the southeastern Pacific, southern Indian Ocean, and southern Atlantic. Another factor that affected the lateral resolution of the phase velocity maps was the choice of the damping made by the authors who opted for maintaining a constant relative model uncertainty for all modes. This too resulted in phase velocity maps of decreasing resolution with increasing overtone number. Visser et al. (2008b) estimated that the fundamental mode 2Ψ terms are resolved up to spherical harmonic degree 8 and degree 5 for the higher modes, which corresponds to a resolving power of about 4500 km near the surface, decreasing to 6500 km near the MTZ. Because the inferences made in this paper focus on large-scale anisotropy, using data of varying resolution should not strongly affect our results. Trade-offs between the different terms of equation 1 constitute another source of uncertainty when constructing anisotropic phase velocity maps from path-averaged measurements. One cannot completely separate the different terms because data coverage is imperfect owing to the uneven distribution of earthquakes and seismic stations over the globe. The resolution matrices calculated by Visser et al. (2008b) showed that these trade-offs were minimal and that there was therefore little mapping of lateral heterogeneities or topography at discontinuities into the anisotropic terms, though one should of course always keep in mind that trade-offs are not completely inexistent.

3 METHOD

3.1 Parameterization

We divided Earth's surface into $10^\circ \times 10^\circ$ cells and the data were inverted by applying the NA to equations 2 and 3 at each grid cell. The reader should note, however, that 10° does not correspond to the lateral resolution of our models since it is directly controlled by the resolution of the phase velocity maps and is limited to larger wavelengths in the deep upper mantle than in the shallow mantle, as discussed in section 2. It is also important to note that the quantitative uncertainty analysis performed in this study does not account for uncertainties stemming from the non-uniform ray path coverage, but is solely focused on the model parameter resolution for a given set of dispersion curves and estimated data uncertainties.

At every grid cell we parameterized $G_c(r)$ and $G_s(r)$ vertically using 12 cubic spline functions $S_i(r)$ (i=1,...,12) of varying depth spacing (Figure 5):

$$G_c(r) = \sum_{i=1}^{12} G_c^i S_i(r) \quad (6)$$

$$G_s(r) = \sum_{i=1}^{12} G_s^i S_i(r) \quad (7)$$

Parameters $B_c(r)$, $B_s(r)$, $H_c(r)$, and $H_s(r)$ are poorly resolved due to the similarity of their partial derivatives (Figure 2), and we therefore opted to neglect them and invert for $G_{c,s}$ only. Most previous authors have either neglected these parameters in surface wave inversions (Marone & Romanowicz 2007) or assumed to be proportional to $G_{c,s}$ (Yao 2015). Such assumptions also enable us to run the NA more efficiently because increasing the number of unknowns quickly raises the computation cost of a model space search. Fig. S1 shows that neglecting the P-wave related parameters does not strongly affect the results for $G_c(r)$ or $G_s(r)$. Under this assumption, equations 2 and 3 become:

$$dc_1(T) = \sum_{i=1}^{12} G_c^i I_i(T) \quad (8)$$

$$dc_2(T) = \sum_{i=1}^{12} G_s^i I_i(T) \quad (9)$$

where

$$I_i(T) = \int S_i(r) K_G(T,r)\, dr \quad (10)$$

In this work, we used a parameterization in terms of relative perturbations $dlnG_{c,s} = G_{c,s}/L$, where L is one of the so-called Love elastic parameter (Love 1927), which determines the wavespeed of vertically polarized shear-waves ($V_{SV} = \sqrt{L/\rho}$). Perturbations are expressed with repect to a local reference model composed of CRUST2.0 (Bassin et al. 2000) and PREM (Dziewonski & Anderson 1981) at each grid cell, as explained in section 3.2.

It should be noted that the spline functions used in this study differ slightly from the ones employed to obtain model YB13SVani (Yuan & Beghein 2013). We therefore cannot fairly compare YB13SVani with our new model resulting from the NA. Thus, in this paper, in addition to presenting the results of a model space search approach (see section 3.3), we display an updated 3-D model obtained using the new splines described above together with the same dataset and singular value decomposition (SVD) method as in Yuan & Beghein (2013). This new model, hereafter referred to as YB17SVaniSVD, is almost identical and display the same features as YB13SVani. Figure 4 shows that the two models are well correlated with one another and they present similar anisotropy amplitudes. Both models display peaks and minima in the root mean square (rms) amplitude and peaks in the gradient of the fast axes at the same depths.

3.2 Effect of the Crust

An important aspect of modeling lateral heterogeneities or anisotropy in the mantle relates to crustal structure. Many first generation 3-D velocity and anisotropy models were obtained using sensitivity kernels calculated based on the 1-D reference mantle model PREM (Dziewonski & Anderson 1981). However, crustal thickness, velocities, and density vary laterally, and neglecting these variations can bias the model due to the mapping of crustal structure into the mantle (Boschi & Ekström 2002; Marone & Romanowicz 2007; Kustowski et al. 2007; Bozdağ & Trampert 2010).

When inverting surface wave data for mantle velocities or anisotropy, it is essential to account for the effect of lateral crustal variations on the sensitivity kernels (Boschi & Ekström 2002; Marone & Romanowicz 2007) and to either correct the data with an *a priori* crustal model (Boschi & Ekström 2002) or invert the data simultaneously for the Moho depth, crustal structure, and mantle structure (Meier et al. 2007; Visser et al. 2008a; Chang et al. 2014). It should, however, be noted that in this last case data uncertainties need to be small to resolve the Moho depth due to trade-offs with velocities (Lebedev et al. 2013). Similarly, when inverting the azimuthally anisotropic part of phase velocity data, one would ideally be able to correct the data for azimuthal anisotropy in the crust or invert the data simultaneously for crust and mantle azimuthal anisotropy. However, to this day there exists no global azimuthal anisotropy model of the crust that we can use to correct the data *a priori*, and because the data used here have little sensitivity to crustal depths, they are likely not sufficient to resolve azimuthal anisotropy in the crust (Figure 3).

We thus used a depth parametrization that averages azimuthal anisotropy in the crust and uppermost part of the mantle (Figure 5), and we accounted for the effect of crustal structure and variations in Moho depth on the $dlnG_{c,s}$ partial derivatives following Yuan & Beghein (2013). More specifically, we generated a local 1-D reference model composed of the PREM mantle to which we superimposed crustal model CRUST2.0 (Bassin et al. 2000) at each grid cell, and calculated the corresponding partial derivatives (Takeuchi 1972). We refer to Yuan & Beghein (2013) for examples of laterally varying sensitivity kernels. The approach taken here is slightly different from that of Yao (2015) who used the isotropic part of the phase velocity maps together with the NA to generate a new local 1-D mantle model. However, we do not expect this to strongly influence our results since it was demonstrated that accounting for lateral variations in mantle structure to calculate the sensitivity kernels does not yield any significant difference in the 3-D azimuthal anisotropy model (Yuan & Beghein 2013).

3.3 The Neighbourhood Algorithm

Model space search techniques are most often applied to non-linear problems, which can be highly non-unique and can have a non-Gaussian cost function with multiple minima. In that case, the solution

obtained by traditional inverse techniques is strongly dependent on prior assumptions and regularization. Forward modeling methods offer a more robust way to solve non-linear problems. They are also useful to solve linear problems since these do not necessarily have Gaussian model parameter distributions (Beghein 2010).

The NA (Sambridge 1999a; Sambridge 1999b) is a guided Monte Carlo search technique that identifies regions of relatively low and relatively high misfit, associated with high and low likelihoods, respectively. For a given parameterization and cost function, if the boundaries of the model space are wide enough, it allows us to map a larger part of the model space (within these selected boundaries) than a damped inversion. In inverse theory, one usually assumes that the prior information on both model and data covariances is Gaussian distributed, which implies a Gaussian distribution of the posterior model covariance (Tarantola 1987). Model space searches, however, enable the user to map the model null-space and to obtain information on the model space approximate topology without having to introduce explicit regularization on the model parameters (e.g. assuming Gaussian prior model distributions) other than the imposed parameterization and the chosen boundaries of the model space being explored. One should also keep in mind that because the imposed range within which we search the parameters is a form of prior information, if this range is very small, it is equivalent to imposing a strong damping. This type of method requires therefore a compromise between efficiency of the model space search and thoroughness of the model space search. In cases like this one, where linearized perturbation theory lies behind the equation employed, one also has to be careful to not sample too wide of a model space which could break the conditions of application of the theory.

The NA is composed of two stages. During the first stage, the model space is sampled randomly, and a cost function is calculated to determined how well each model explains the data. At each iteration, the number of models generated increases in the vicinity of the best fitting regions of the model space. The first stage of the NA differs from many other Monte Carlo techniques in that its objective is not to locate a single optimal model, but to obtain an overview of the model space. It therefore keeps track of all the models generated instead of discarding the worse data fitting models at each iteration.

The cost function $\phi(m)$ employed in this study to drive the sampling is defined as:

$$\phi(m) = \frac{1}{N} \sum_{i=1}^{N} \left(\frac{d_i - (Am)_i}{\sigma_i} \right)^2 \tag{11}$$

where N is the total number of data, m_i is the ith component of the model vector $\mathbf{m}$ generated by the NA, d_i is the ith component of the data vector $\mathbf{d}$ and $(Am)_i$ is the ith component of the vector $\mathbf{Am}$ containing the data predictions calculated using equations 2 or 3 and the sensitivity kernels projected onto the spline functions. σ_i is the error in the phase velocity maps estimated by Visser et al. (2008b). Note that equation 11 assumes that data uncertainties follow Gaussian distributions. In addition, it

is good to remind the reader that these standard deviations result from global inversions of path-averaged phase velocity measurements and are therefore, in fact, posterior errors on the phase velocity dispersion curves that we use here to build a prior data covariance matrix.

In this work, we solved the problem for dc_1 and dc_2 separately at each grid cell, i.e. we ran the NA $36 \times 18 = 648$ times for dc_1 and 648 times for dc_2, searching the model space for 12 spline parameters each time. Each model parameter ($dlnG^i_{c,s}$ for $i = 1, ..., 12$) was allowed to vary uniformly between -0.03 and $+0.03$ around model YB17SVaniSVD, which resulted from a regularized inversion as explained in section 3.1. This range was selected to allow most parameters to change sign if required by the data. We tested that running the NA around PREM (for which all $dlnG^i_{c,s}$ are zero) does not affect the outcome of the model space search provided convergence is achieved and a broad enough model space search is performed (Figures S2 and S3). Running the model exploration around YB17SVaniSVD was, however, more computationally efficient because the sampling started from a reasonably good data-fitting model, enabling faster convergence in cases where the model space topography was approximately Gaussian. Nevertheless, doing so did not prevent the NA to find other solutions, away from the starting model, because we insured the model space search was broad and thorough using multiple tests and settings in the NA algorithm.

In a second stage, a Bayesian appraisal of all the models is performed. Unlike other statistical techniques, such as importance sampling, that draw inferences on the models using only a subset of the ensemble of models generated, the NA makes use of all the models, good and bad, generated during the first stage. As pointed out by Sambridge (1999b), in some cases one can learn from the models that fit the data poorly as much as from those that fit the data well. The entire family of models obtained in the first stage is thus converted into posterior probability density functions (PPDFs) by associating the relatively low and high misfit values to high and low likelihoods, respectively. These PPDFs can be used to assess the robustness of the model parameters.

For a PPDF denoted by $P(\mathbf{m})$ where $\mathbf{m}$ is a point in the model space, the posterior mean model for the ith parameter is given by the following integral performed over the model space (Sambridge 1999b):

$$< m_i >= \int m_i P(\mathbf{m}) d\mathbf{m} \tag{12}$$

The posterior variances of the model parameters can be obtained from the diagonals of the posterior model covariance matrix given by:

$$C_{i,j} = \int m_i m_j P(\mathbf{m}) d(\mathbf{m}) - < m_i >< m_j > \tag{13}$$

Because the model space, including the null-space, was sampled, the model uncertainties inferred are more accurate than those resulting from regularized inversions. Those result from the local curvature

of the cost function around a model chosen with an explicit regularization and assuming Gaussian statistics. However, if the underlying statistics are not Gaussian or if the cost function has a wide valley (e.g., if the null-space is large), error estimates from regularized inversions underestimate the posterior model variance (Trampert 1998; Beghein & Trampert 2003; Beghein 2010). An example of model uncertainties estimated with the NA compared to those resulting from an inversion by SVD (Menke 2012) is shown in Figure S4.

The 1-D marginal distribution of a given model parameter m_i can be obtained by integrating $P(\mathbf{m})$ numerically over all other parameters (Sambridge 1999b):

$$M(m_i) = \int ... \int P(\mathbf{m}) \prod_{k=1,k\neq i}^{d} dm_k \tag{14}$$

where d is the total number of model parameters. The shape and width of these 1-D marginals provide useful information on how well constrained a given parameter is and whether the model distribution is Gaussian, in which case the mean $< m_i >$ coincides with the peak of the distribution, i.e. the most likely value. Information about parameter trade-offs can be obtained from the diagonal terms of the posterior covariance matrix, and from the 2-D marginal distributions, which are calculated by integrating $P(\mathbf{m})$ over all but two parameters. The 2-D marginal PPDF for the ith and jth parameters is given by:

$$M(m_i, m_j) = \int ... \int P(\mathbf{m}) \prod_{k=1,k\neq i,k\neq j}^{d} dm_k \tag{15}$$

Figure 6 displays a representative example of 1-D and 2-D marginals. No trade-off is visible between the spline parameters displayed, and we checked that this was the case for other pairs of G_c and G_s parameters at several grid cells. From the PPDFs of these $G^i_{c,s}$ spline parameters, we can reconstruct probability distributions for G_c and G_s as a function of depth by:

(i) Drawing $10,000$ random values for each of the $G^i_{c,s}$ ($i = 1, ..., 12$) coefficients from their posterior 1-D marginal distributions;

(ii) For each set of $G^i_{c,s}$ values, calculate the $G_{c,s}(r)$ profile (equations 6 for $G_c(r)$ and 7 for $G_s(r)$), which results in $10,000$ $G_{c,s}(r)$ models

This yields distributions of $dlnG_c(r)$ and $dlnG_s(r)$ models drawn directly from the G^i_c and G^i_s PPDFs at each grid cell. An example is shown in Figure 7. We note that the mean models as identified by the NA do not necessarily coincide with the inversion results, and that the data generally favor larger amplitudes than obtained from a regularized inversion. It should also be pointed out that the mean model does not necessarily correspond to the best fitting model since not all PPDFs are Gaussian. This is why it is important to not discuss the mean model alone, but to account for its uncertainties.

Finally, the reader should note that the existence of discontinuities in seismic velocities in the local reference models was shown to not be responsible for changes in G_c and G_s by Yuan & Beghein (2013).

3.4 Error Propagation

To evaluate the robustness of the features observed in a tomographic model such as YB13SVani (Yuan & Beghein 2013) or YB17SVaniSVD, we ideally need to determine the mean amplitude $dlnG$ and mean fast axis direction Θ at each depth and at each grid cell together with their respective uncertainties. However, the formulation of the linearized forward problem described in section 2 does not allow us to model $dlnG$ and Θ directly. Previous attempts at estimating model uncertainties on azimuthal anisotropy with the NA (Yao 2015) have focused on the G_c and G_s uncertainties, and only discussed the azimuthal anisotropy ($dlnG$ and Θ) model resulting from the most likely or mean G_c and G_s only. Because we adopted a Bayesian approach in this study, posterior uncertainties on $dlnG$ and Θ can, however, be transmitted from the $dlnG_c$ and $dlnG_s$ model distributions, as explained below.

One approach consists in calculating $dlnG$ and Θ distributions by (1) drawing models from the PPDFs of the individual $dlnG_c(r)$ and $dlnG_s(r)$ profiles (Figure 7), and (2) calculating $dlnG(r)$ and $\Theta(r)$ for each pair of $dlnG_c(r)$ and $dlnG_s(r)$ model drawn. This would yield distributions of $dlnG(r)$ and $\Theta(r)$ models drawn directly from the $dlnG_c$ and $dlnG_s$ PPDFs. A similar method was taken by Beghein & Trampert (2004a) and Visser et al. (2008a) for radial anisotropy. One can then derive a mean and standard deviation from the reconstructed PPDFs, though we point out that they might not be Gaussian. In our case, however, this technique yields a mean model that has little to do with the model that results from the best fitting $dlnG_c$ and $dlnG_s$ because of the higlhy non-Gaussian nature of the resulting $dlnG$ and Θ PPDFs. The interpretation of the model and its error bars is thus extremely challenging as demonstrated in Figs. S5-S7.

We opted for another approach instead, involving the propagation of the errors obtained from the individual $dlnG_c(r)$ and $dlnG_s(r)$ PPDFs. This approach assumes the PPDFs are Gaussian distributed, which is clearly an approximation for some parameters (Figures 6 to 7), but it enables us to avoid possible artifacts such as those seen in the synthetic examples. Let us take a function f that depends on parameters x and y that are assumed to be Gaussian with standard deviations σ_x and σ_y, respectively. If we further assume that the x and y variables have no covariance, the variance σ_f^2 of function f depends on the variances σ_x^2 and σ_y^2 of x and y as follows (Clifford 1973):

$$\sigma_f^2 = \left(\frac{\partial f}{\partial x}\right)^2 \sigma_x^2 + \left(\frac{\partial f}{\partial y}\right)^2 \sigma_y^2 \tag{16}$$

Therefore, for $f = G = \sqrt{G_s^2 + G_c^2}$, we can determine that :

$$\sigma_G^2 = \frac{G_s^2\sigma_{G_s}^2 + G_c^2\sigma_{G_c}^2}{G_s^2 + G_c^2} \tag{17}$$

And for $f = \Theta = \frac{1}{2}\arctan(G_s/G_c)$:

$$\sigma_\Theta^2 = \frac{1}{4}\frac{G_c^2\sigma_{G_s}^2 + G_s^2\sigma_{G_c}^2}{(G_s^2 + G_c^2)^2} \tag{18}$$

Here, we used $G_c = G_{c,mean}$ and $G_s = G_{s,mean}$ as determined from equation 12 and the variances $\sigma_{G_c}^2$ and $\sigma_{G_s}^2$ result from the off-diagonals of the posterior covariance matrix (equation 13). The uncertainty maps displayed in section 4 were determined from these error propagation calculations. We assumed no covariance between G_s and G_c, which is a reasonable approximation since Visser et al. (2008b) showed there was little covariance between the dc_1 and dc_2 terms of equation 1.

4 RESULTS AND DISCUSSION

4.1 Goodness of Fit

Figure 8 compares some of the azimuthally anisotropic phase velocity maps measured by Visser et al. (2008b) with predictions from the model resulting from our regularized inversion (YB17SVaniSVD) and from the mean NA model, i.e. the model corresponding to the mean of the $G_c(r)$ and $G_s(r)$ distributions. We see that both models can generally reproduce the data well and that the discrepancies are mostly in the amplitudes and less so in the fast axes directions. This figure also shows that a NA inversion for G only can yield a model that fits the data as well as a model obtained by regularized inversion for parameters B, G, and H.

Following Yuan & Beghein (2014), we calculated an average χ^2 misfit by averaging the χ^2 from the G_c model (χ_c^2) and from the G_s model (χ_s^2) over all grid cells:

$$\chi_{c,s}^2 = \frac{1}{N}\sum_{i=1}^{N}\left(\frac{d_i - (Am)_i}{\sigma_i}\right)^2 \tag{19}$$

$$\chi^2 = \frac{1}{N_c}\sum_{i=1}^{N_c}\left(\chi_{c,i}^2 + \chi_{s,i}^2\right) \tag{20}$$

where N is the total number of data, d_i is the ith component of the data vector $\mathbf{d}$, σ_i is the ith component of the vector containing data errors, and $(Am)_i$ is the ith component of the data prediction vector $\mathbf{Am}$ calculated using equations 8 and 9. N_c is the total number of grid cells. Table 1 gives the average χ^2 misfit for each model, and confirms that the two models can explain the data within uncertainties.

Table 2 compares the average variance reduction for the two models, using the following definition of the variance reduction:

$$VR = 1 - \frac{\sum_{i=1}^{N} (d_i - (Am)_i)^2}{\sum_{i=1}^{N} d_i^2} \quad (21)$$

It shows that model YB17SVaniSVD explains 94 % of the data, and the mean NA model explains 79 % of the data. We attribute the better data fit of YB17SVaniSVD compared to the mean NA model to the fact that the mean NA model does not correspond exactly to one of the best data-fitting models due to the non-Gaussian nature of the posterior model 1-D distributions.

4.2 Global Averages

Some of the most interesting features detected in YB13SVani (Yuan & Beghein 2013) were the changes in the average azimuthal anisotropy fast directions associated with amplitude minima at about 220 km depth, and near the MTZ boundaries. While the interpretation of these results is non-unique because too few mineral physics data are available on the anisotropy of MTZ material, these results provide new constraints on deep upper mantle circulation, and the observed changes in anisotropy at the MTZ boundaries could be the signature of changes in mantle flow direction. To determine whether our new results confirm these findings, we determined the vertical gradient of the fast axes ($d\Theta/dr$) and the relative anisotropy amplitude ($d \ln G$) at each grid cell every 10 km depth with a 20 km window, after which we calculated their root mean square (rms) as a function of depth, following Yuan & Beghein (2013) Figure 9 represents the rms of $d \ln G$ and of $d\Theta/dr$ calculated for the mean NA model and for YB17SVaniSVD.

We see that even though the 1-D average of the mean NA model presents a few more oscillations below 300 km depth than the model obtained by regularized inversion, the two models display similar features. We observe 1.5 % to 2 % anisotropy in the top 200 km and about 1 % below, down to at least the bottom of the MTZ. We also detect amplitude minima between 50 km and 100 km, around 220 km and 250 km, and near the boundaries of the MTZ. These minima are associated with higher gradients in the fast axes direction, as observed in YB13SVani.

Note that in Yuan & Beghein (2013) we demonstrated that these changes in anisotropy are not artifacts due to the presence of discontinuities in seismic velocities in the local reference models, and that they were stable with respect to regularization and with respect to the presence of lateral heterogeneities in the mantle. We also previously demonstrated (Yuan & Beghein 2013; Yuan & Beghein 2014) that the model does not depend on the choice of the spline functions, the position of their peaks, or their spacing. The robustness of these features is of course better tested with quantitative model uncertainties, but these are difficult to display for $rms(dlnG)$ and $rms(d\Theta/dr)$. We decided to focus on the uncertainties of the 3-D model instead (see below).

4.3 3-D Models

In this section, we discuss the 3-D models obtained with the NA and compare them with YB17SVaniSVD. Figure 10 shows the correlation coefficient between the two models as a function of depth. It was calculated after expansion of each model map in generalized spherical harmonics up to degree 20, following Yuan & Beghein (2014). At all depths, the correlation is well above the 95 % significance level as calculated by Becker et al. (2007), demonstrating that the two models are overall consistent with one another.

Figures 11 to 14 are maps that represent model YB17SVaniSVD and the NA results at different depths. In Figures 11 and 12, both the mean NA model and the fast axes standard deviation are displayed. The fast axes standard deviation was estimated at each grid cell with equation 18. Figures 13 and 14 focus on the anisotropy amplitude and its standard deviation (equation 17). The two models show very similar fast axes directions at most depths and comparable amplitudes. They are also consistent with previous studies in the top 200 km (Nishimura & Forsyth 1989; Montagner & Tanimoto 1991; Debayle et al. 2005). Differences in model amplitudes are generally within the model uncertainties (e.g. differences in the anisotropy pattern in the western Pacific at 100 km between YB17SVaniSVD and Debayle and Ricard (2013) or Becker et al. (2014)). We note, however, that the large amplitudes seen in the Debayle and Ricard (2013) model in the uppermost mantle are difficult to reconcile with our results, even accounting for the posterior model variance, except near the South American subduction zone and at the Eurasia-Africa boundary.

The strongest model amplitudes (of at least 2 % to 3 % anisotropy) in the top 150 km of our model are well resolved and can be found in the youngest parts of the Pacific plate, at the Africa-Eurasia plate boundary, and around the South American subduction zone. Lower amplitudes are seen in the western Pacific at these depths. These low amplitudes were first detected by Nishimura & Forsyth (Nishimura & Forsyth 1989) who related them to changes in the horizontal direction of anisotropic fabric with depth rather than being due to a decrease of in situ anisotropy. In Yuan & Beghein (2014), we showed, however, that the lower SV anisotropy amplitude in the western Pacific is close to the average amplitudes of other oceanic plates and is therefore not anomalously low with respect to other plates. We also note that while seismic anisotropy amplitudes are anomalously high in the shallow mantle in the middle of the Pacific plate, it is one of the places where the amplitude is the weakest at greater depths, suggesting a relatively shallow origin for this signal, such as asthenospheric mantle flow. This was previously suggested for radial anisotropy models (Ekström & Dziewonski 1998; Gaboret et al. 2003). We also find a relatively strong signal of about 3 % anisotropy at 100 km depth near the India-Eurasia convergence zone and in the Indonesian subduction region. Amplitude uncertainties are closer to the mean model amplitudes at greater depths, except in a few locations

between 200 km and 350 km such as the Western part of the Pacific where subduction occurs, near the Arabian plate, and India. Below 350 km depth, a stronger, well-resolved signal appears in the northwestern part of the Pacific and Asia.

Strong discrepancies were found between model YB13SVani (Yuan & Beghein 2013) and the uppermost mantle model of Marone & Romanowicz (2007) under North America. We had attributed this disagreement to differences in the horizontal resolution of the models (Yuan & Beghein 2013). Here, we see that the uncertainties in the fast axes directions at 100 km are strong beneath this region, which would reconcile the differences between the models. Uncertainties on the fast axes are also slightly stronger toward the western part of the Pacific. As we go deeper, more regions display larger standard deviations in the fast axes direction, but a few features appear well constrained. For instance, the fast seismic direction is close to the absolute plate motion (Gripp & Gordon 2002) beneath the young and mid Pacific plate down to about 150 km depth (Figure 15), though model YB17SVaniSVD appears to reflect the plate motion slightly better than the mean NA model (see for instance in the younger parts of the Pacific plate). This is attributed to the fact that the mean model is not necessarily the best fitting model due to the non-Gaussian topology of the model space, as explained above. We do not expect other reference frames to yield a better alignment with the anisotropy since our new models are very similar to YB13SVani, which had been tested against other APM models (Yuan & Beghein 2013).

A question that arises from Fig. 9 is whether the changes in azimuthal anisotropy at the MTZ boundaries are global or appear only at a few locations. If they occur globally, they might be caused purely by the effect of pressure on MTZ material anisotropy. If they occur only in a few regions, compositional effects might come into play. To try to answer this question, one can make a simple visual comparison of the model maps at different depths. It is, however, important to keep in mind when comparing maps that not all grid cells have well resolved fast directions and that the phase velocity maps may have been affected by small trade-offs between isotropic and anisotropic anomalies. We thus took advantage of the fact that the forward modeling method used here yielded quantitative posterior model uncertainties and plotted the anisotropy only at locations where the fast direction was best resolved. This is displayed in Fig. 16 for depths of 350 km, 450 km, 600 km, and 700 km. They represent the fast direction at grid cells where the error on Θ was less than $45°$. This is a subjective cutoff value, but looking at smaller cutoff values (e.g. $35°$) did not change our conclusions. Visual inspection of these maps shows that there is little variations of the fast seismic direction across depths in the general area where the Pacific plate subducts underneath the North American plate and under the Philippine plate. The same is also true, for instance, around the South American subduction zone,

between the Arabian and Eurasian plates, in the Southeastern Pacific, and where the Indian, African and Indo-Australian plates meet.

Another way of looking at this is by calculating the difference between the fast direction at depths above and below the MTZ boundaries. This is what is represented in Fig. 17. It shows the difference between the mean fast directions at 350 km and 450 km and between depths of 600 km and 700 km at all grid cells and for spherical harmonic degrees 1-5, which is the estimated lateral resolution for azimuthal anisotropy at these depths (see section 2). While one might be tempted to conclude from Fig. 16 that subduction zones are characterized by the same fast direction across the MTZ, there is no clear pattern relating to surface tectonics visible in Fig. 17. Nevertheless, from the degree 5 maps, one can conclude that regions such as Africa, Asia, and the northwestern Pacific are characterized by similar azimuthal anisotropy above, below, and inside the MTZ. Thus, even though the lateral resolution of the higher modes and posterior model uncertainties do not allow us to determine with high precision where the fast axes do and do not change at MTZ depths, our results suggest that the change in fast direction across the MTZ boundaries is not likely to occur globally and is thus not solely due to pressure effects.

5 CONCLUSIONS

The goal of this research was to present a new method to model and obtain quantitative uncertainties on 3-D azimuthal seismic anisotropy. It was applied to global higher mode surface wave phase velocity data to assess the likelihood of azimuthal anisotropy in the deep upper mantle. For this, we employed the Neighbourhood Algorithm developed by Sambridge (1999a; 1999b), a model space search approach that enables searching a broader part of the model space than a damped inversion, including the null space. Even though the linearized formulation of the problem relating phase velocities to azimuthal anisotropy at depth does not allow us to directly obtain uncertainties on the anisotropy amplitude and fast axes direction, we showed that that they can be determined *a posteriori*.

The PPDFs of the resulting models yielded a mean model that was overall consistent (correlation above the 95 % significance level) with models obtained by regularized inversion with the same dataset and parameterization, but with somewhat larger amplitudes. The posterior model variance was also larger than estimates from regularized inversions, which is to be expected in the presence of a large model null-space. We confirm our previously published results showing that azimuthal anisotropy of 1-2 % is present in the MTZ and that, on average, the anisotropy changes across the MTZ boundaries. This change is therefore required by the higher mode data utilized, and did not result from inversion artefact or parameter trade-offs that could have affected our previous model, YB13SVani. We showed, however, that the anisotropy change across the MTZ boundaries is liklely not a global feature, but

further studies will be required to improve the lateral resolution of the models at those depths and determine whether there is any relation between the change (or lack thereof) of anisotropy across the 410- and 670-discontinuities.

ACKNOWLEDGMENTS

We wish to thank Karin Visser and Jeannot Trampert for making the phase velocity maps freely available online at `http://www.geo.uu.nl/~jeannot/My_web_pages/Downloads.html`, and Malcom Sambridge for sharing his Neighbourhood Algorithm. Anonymous reviewers and editorial comments helped improve this manuscript. Partial derivatives were calculated using program MINEOS (available on the CIG website at `http://www.geodynamics.org/`), and figures were made using the Generic Mapping Tool and Gnuplot. This research was partially funded by NSF EAR grants 0838605 and 0949255.

REFERENCES

Auer, L., Boschi, L., Becker, T., Nissen-Meyer, T., & Giardini, D., 2014. Savani: A variable resolution whole-mantle model of anisotropic shear velocity variations based on multiple data sets, *J. geophys. Res.*, **119**(4), 3006-3034, doi:10.1002/2013JB010773

Bassin, C., Laske, G. & Masters, G., 2000. The Current Limits of Resolution for Surface Wave Tomography in North America, *EOS*, **81**, F897

Becker, T. W., Kellogg, J. B., Ekström, G., & O'Connell, R. J., 2003. Comparison of azimuthal seismic anisotropy from surface waves and finite strain from global mantle-circulation models, *Geophys. J Int.*, **155**(2), 696-714, doi:10.1046/j.1365-246X.2003.02085.x

Becker, T. W., Ekström, G., Boschi, L., & Woodhouse, J. D., 2007. Length scales, patterns and origin of azimuthal seismic anisotropy in the upper mantle as mapped by Rayleigh waves, *Geophys. J Int.*, **171**(1), 451-462, doi:10.1111/j.1365-246X.2007.03536.x

Becker, T. W., Conrad, C.P., Schaeffer, A.J., & Lebedev, S., 2014. Origin of azimuthal seismic anisotropy in oceanic plates and mantle, *Earth Planet. Sci. Lett.*, **401**(1), 236-250, doi:10.1016/j.epsl.2014.06.014

Beghein, C., 2010. Radial anisotropy and prior petrological constraints: A comparative study, *J. geophys. Res.*, **115**, B03303, doi:10.1029/2008JB005842

Beghein, C. & Trampert, J., 2003. Robust normal mode constraints on inner-core anisotropy from model space search, *Science*, **299**, 552-555, doi:10.1126/science.1078159

Beghein, C. & Trampert, J., 2004a. Probability density functions for radial anisotropy from fundamental mode surface wave data and the neighbourhood algorithm, *Geophys. J Int.*, **157**, 1163-1174, doi:10.1111/j.1365-246X.2004.02235.x

Beghein, C. & Trampert, J., 2004b. Probability density functions for radial anisotropy: Implications for the upper 1200 km of the mantle, *Earth Planet. Sci. Lett.*, **217**, 151-162, doi:10.1016/S0012-821X(03)00575-2

Beghein, C., Resovsky, J., & Trampert, J., 2002. P and S tomography using normal mode and surface wave data with a Neighbourhood Algorithm, *Geophys. J Int.*, **149**(3), 646-658, doi:10.1046/j.1365-246X.2002.01684.x

Beghein, C., Trampert, J., & van Heijst, H. J., 2006. Radial anisotropy in seismic reference models of the mantle, *J. geophys. Res.*, **111**, B02303, doi:10.1029/2005JB003728

Beghein, C., Resovsky, J., & van der Hilst, R. D., 2008. The signal of mantle anisotropy in the coupling of normal modes, *Geophys. J Int.*, **175**(3), 1209-1234, doi:10.1111/j.1365-246X.2008.03970.x

Beghein, C., Yuan, K., Schmerr, N., & Xing, Z., 2014. Changes in seismic anisotropy shed light on the nature of the Gutenberg discontinuity, *Science*, **343**, 1237-1240, doi:10.1126/science.1246724

Boschi, L., & Ekström, G., 2002. New images of the Earth's upper mantle from measurements of surface wave phase velocity anomalies, *J. geophys. Res.*, **107**, B4, doi:10.1029/2000JB000059

Bozdağ, E. & Trampert, J., 2010. Assessment of tomographic mantle models using spectral element seismograms, *Geophys. J Int.*, **180**(3), 1187-1199, doi:10.1111/j.1365-246X.2009.04468.x

Chang, S., Ferreira, A., Ritsema, J., van Heijst, H., & Woodhouse, J. H., 2014. Global radially anisotropic mantle structure from multiple datasets: A review, current challenges, and outlook, *Tectonophysics*, **617**, 1-19, doi:10.1016/j.tecto.2014.01.033

Chen, W. P. & Brudzinski, M. R., 2003. Seismic anisotropy in the mantle transition zone beneath Fiji-Tonga, *Geophys. Res. Lett.*, **30**(13), 1682, doi:10.1029/2002GL016330

Clifford, A.A., 1973. Multivariate error analysis: a handbook of error propagation and calculation in many-parameter systems, Wiley, New York.

Debayle, E. & Ricard, Y., 2013. *Seismic observations of large-scale deformation at the bottom of fast-moving plates*, *Earth Planet. Sci. Lett.*, **376**, 165-177, doi:10.1016/j.epsl.2013.06.025

Debayle, E., Kennett, B., & Priestley, K., 2005. Global azimuthal seismic anisotropy and the unique plate-motion deformation of Australia, *Nature*, **433**(7025), 509-512, doi:10.1038/nature03247

Dziewonski, A. M. & Anderson, D. L., 1981. Preliminary reference Earth model, *Phys. Earth Planet. Inter.*, **25**(4), 297-356, doi:10.1016/0031-9201(81)90046-7

Ekström, G., 2011. A global model of Love and Rayleigh surface wave dispersion and anisotropy, 25-250 s, *Geophys. J Int.*, **187**(3), 1668-1686, doi:10.1111/j.1365-246X.2011.05225.x

Ekström, G., & Dziewonski, A. M., 1998. The unique anisotropy of the Pacific upper mantle, *nature*, **394**(6689), 168-172, doi:10.1038/28148

Foley, B. J. & Long, M. D., 2011. Upper and mid-mantle anisotropy beneath the Tonga slab, *Geophys. Res. Lett.*, **38**(2), L02303, doi:10.1029/2010GL046021

Fouch, M. J. & Fischer, K. M., 1996. Mantle anisotropy beneath northwest Pacific subduction zones, *J. geophys. Res.*, **101**(B7), 15987-16002, doi:10.1029/96JB00881

French, S. W. & Romanowicz, B., 2014. Whole-mantle radially anisotropic shear velocity structure from

spectral-element waveform tomography, *Geophys. J Int.*, **199**(3), 1303-1327, doi:10.1093/gji/ggu334

Gaboret, C., Forte, A.M., & Montagner, J.-P., 2003. The unique dynamics of the Pacific Hemisphere mantle and its signature on seismic anisotropy, *Earth Planet. Sci. Lett.*, **208**(3-4), 219-233, doi:10.1016/S0012-821X(03)00037-2

Gripp, A.E. & Gordon, R.G., 2002. Young tracks of hotspots and current plate velocities, *Geophys. J Int.*, **150**(2), 321-361, doi:10.1046/j.1365-246X.2002.01627.x

Hu, X.-G., Xue, X.-X., Liu, L.-T., & Sun, H.-P., 2012. Normal mode coupling due to azimuthal anisotropy in the transition zone: an example from Taiwan Island, *Geophys. J Int.*, **190**(1), 323-334, doi:10.1111/j.1365-246X.2012.05463.x

Karato, S., 1998. Seismic anisotropy in the deep mantle, boundary layers and the geometry of mantle convection, *Pure Appl. Geophys.*,**151**(2-4), 565-587, doi:10.1007/s000240050130

Karato, S., Zhang, S., & Wenk, H.-R., 1995. Superplasticity in Earth's lower mantle - evidence from seismic anisotropy and rock physics, *S*cience, **270**(5235), 458-461, doi:10.1126/science.270.5235.458

Karato, S.-i., 1989. Seismic anisotropy: Mechanisms and tectonic implications, in *Rheology of Solids and of the Earth*, pp. 393-422, eds Karato, S.-I. & Toriumi, M., Oxford University Press, New York.

Kendall, J.-M. & Silver, P. G., 1996. Constraints from seismic anisotropy on the nature of the lowermost mantle, *Nature*, **381**(6581), 409-412, doi:10.1038/381409a0

Kosarian, M., and Davis, P. M., Tanimoto, T., & Clayton, R. W., 2011. The relationship between upper mantle anisotropic structures beneath California, transpression, and absolute plate motions, *J. geophys. Res.*, **116**(B8), B08307, doi:10.1029/2010JB007742

Kustowski, B., Dziewonski, A., & Ekström, G., 2007. Nonlinear crustal corrections for normal-mode seismograms, *Bull. seism. Soc. Am.*, **97**(5), 1756-1762, doi:10.1785/0120070041

Kustowski, B., Ekström, G., & Dziewonski, A., 2008. Anisotropic shear-wave velocity structure of the Earth's mantle: A global model, *J. geophys. Res.*, **113**(B6), B06306, doi:10.1029/2007JB005169

Lebedev, S., Adam, J.M.C., & Meier, T., 2008. Mapping the Moho with seismic surface waves: A review, resolution analysis, and recommended inversion strategies, *Tectonophysics*, **609**(C), 377-394, doi:10.1016/j.tecto.2012.12.030

Lynner, C. & Long, M. D., 2015. Heterogeneous seismic anisotropy in the transition zone and uppermost lower mantle beneath Japan, Izu-Bonin, and South America, *Geophys. J Int.*, **201**, 1545-1552, doi:10.1093/gji/ggv099

Long, M. D., 2013. Constraints on subduction geodynamics from seismic anisotropy, *Rev. Geophys.*, **51**(1), 76-112, doi:10.1002/rog.20008

Love, A. E. H. , 1927. A Treatise on the Mathematical Theory of Elasticity, Cambridge University Press, Cambridge

Marone, F. & Romanowicz, B., 2007. The depth distribution of azimuthal anisotropy in the continental upper mantle, *Nature*, **447**(7141), 198-201, doI:10.1038/nature05742

Matsu'ura, M. and Hirata, N., 1982. Generalized least-squares solutions to quasi-linear inverse problems with a

priori information, *Journal of Physics of the Earth*, **30**(6), 451-468, doi:10.4294/jpe1952.30.451

Maupin, V., Garnero, E. J., Lay, T., & Fouch, M. J., 2005. Azimuthal anisotropy in the D" layer beneath the Caribbean, *J. geophys. Res.*, **110**, B08301, doi:10.1029/2004jb003506

Meier, U., Curtis, A., & Trampert, J., 2007. Global crustal thickness from neural network inversion of surface wave data, *Geophys. J Int.*, **169**(2), B706-722, doi:10.1111/j.1365-246X.2007.03373.x

Menke, W. , 2012. Geophysical Data Analysis: Discrete Inverse Theory, Third edition, Elsevier, 330 p., ISBN:978-0-12-397160-9.

Montagner, J.-P., 1994. Can seismology tell us anything about convection in the mantle?, *Rev. Geophys.*, **32**(2), 115-137, doi:10.1029/94RG00099

Montagner, J.-P., and Nataf, H.-C., 1986. A simple method for inverting the azimuthal anisotropy of surface waves, *J. geophys. Res.*, **91**, 511-520, doi:10.1029/JB091iB01p00511

Montagner, J.-P. & Tanimoto, T., 1991. Global upper mantle tomography of seismic velocities and anisotropies, *J. geophys. Res.*, **96**, B12, 20337-20351, doi:10.1029/91JB01890

Montagner, J.-P., and Kennett, B.L.N., 1996. How to reconcile body-wave and normal-mode reference Earth models, *Geophys. J Int.*, **125**(1), 229-248, doi:10.1111/j.1365-246X.1996.tb06548.x

Moulik, P. & Ekström, G., 2014. An anisotropic shear velocity model of the Earth's mantle using normal modes, body waves, surface waves and long-period waveforms, *Geophys. J Int.*, **199**(3), 1713-1738, doi:10.1093/gji/ggu356

Nicolas, A. & Christensen, N., 1987. Formation of anisotropy in upper mantle peridotites - a review, in *Composition, Structure, and Dynamics of the Lithosphere-Asthenosphere System*, eds Fuchs, A. & Froideveaux, C., American Geophysical Union, Washington, D. C.. doi: 10.1029/GD016p0111

Nishimura, C. E. & Forsyth, D. W., 1988. Rayleigh wave phase velocities in the Pacific with implications for azimuthal anisotropy and lateral heterogeneities, *Geophys. J Int.*, **94**(3), 479-501, doi:10.1111/j.1365-246X.1988.tb02270.x

Nishimura, C. E. & Forsyth, D. W., 1989. The anisotropic structure of the upper mantle in the Pacific, *Geophysical Journal*, **96**(2), 203-229, doi:10.1111/j.1365-246X.1989.tb04446.x

Nowacki, A., Kendall, J.-M., Wookey, J., & Pemberton, A., 2015. Mid-mantle anisotropy in subduction zones and deep water transport, *Geochemistry, Geophysics, Geosystems*, **16**, 764-784, doi:10.1002/2014GC005667

Oganov, A., 2005. Anisotropy of Earth's D" layer and stacking faults in the $MgSiO_3$ post-perovskite phase, *Nature*, **438**, 1142-1144, doI:10.1038/nature04439

Panning, M. & Romanowicz, B., 2004. Inferences on Flow at the Base of Earth's Mantle Based on Seismic Anisotropy, *Science*, **303**(351), 351-353, doi:10.1126/science.1091524

Panning, M. & Romanowicz, B., 2006. A three-dimensional radially anisotropic model of shear velocity in the whole mantle, *Geophys. J Int.*, **167**(1), 361-379, doI:10.1111/j.1365-246X.2006.03100.x

Panning, M. P., Lekić, V., & Romanowicz, B., 2010. Importance of crustal corrections in the development of a new global model of radial anisotropy, *J. geophys. Res.*, **115**(B12), B12325, doI:10.1029/2010JB007520

Romanowicz, B. & Lekić, V., 2011. Inferring upper-mantle structure by full waveform tomography with the spectral element method, *Geophys. J Int.*, **185**(2), 799-831, doi:10.1111/j.1365-246X.2011.04969.x

Sambridge, M., 1999a. Geophysical inversion with a neighbourhood algorithm - I. Searching a parameter space, *Geophys. J Int.*, **138**(2), 479-494, doi:10.1046/j.1365-246X.1999.00876.x

Sambridge, M., 1999b. Geophysical inversion with a neighbourhood algorithm - II. Appraising the ensemble, *Geophys. J Int.*, **138**(3), 727-746, doi:10.1046/j.1365-246x.1999.00900.x

Schaeffer, A.J., Lebedev, S., & Becker, T. W., 2016. Azimuthal seismic anisotropy in the Earth's upper mantle and the thickness of tectonic plates, *Geophys. J Int.*, **207**(2), 901-933, doi:10.1093/gji/ggw309

Silver, P. G., 1996. Seismic anisotropy beneath the continents: Probing the Depths of Geology, *Ann. Rev. Earth Planet Sci.*, **24**(1), 385-432, doi:10.1146/annurev.earth.24.1.385

Smith, D. B., Ritzwoller, M. H., & Shapiro, N. M., 2004. Stratification of anisotropy in the Pacific upper mantle, *J. geophys. Res.*, **109**(B11), doi:10.1029/2004JB003200

Snoke, J. A. & Sambridge, M., 2002. Constraints on the S wave velocity structure in a continental shield from surface wave data: Comparing linearized least squares inversion and the direct search Neighbourhood Algorithm, *J. geophys. Res.*, **107**(B5), doi:10.1029/2001JB000498

Takeuchi, H. & Saito, M. 1972. *Seismic surface waves*, in Methods in Computational Physics, pp. 217-295, ed. Bolt B., Academic Press, New York.

Tarantola, A., 1987. *Inverse Problem Theory and Methods for Model Parameter Estimation*, Elsevier, New York.

Trampert, J., 1998. Global seismic tomography: the inverse problem and beyond, *Inverse Problems*, **14**, 371-385, doi:10.1088/0266-5611/14/3/002

Trampert, J. & van Heijst, H. J., 2002. Global Azimuthal Anisotropy in the Transition Zone, *Science*, **296**(5571), 1297-1299, doi:10.1126/science.1070264

Trampert, J. & Woodhouse, J. H., 2003. Global anisotropic phase velocity maps for fundamental mode surface waves between 40 and 150 s, *Geophys. J Int.*, **154**(1), 154-165, doi:10.1046/j.1365-246X.2003.01952.x

Visser, K., Trampert, J., and Kennett, B. L. N., 2008b. Global anisotropic phase velocity maps for higher mode Love and Rayleigh waves, *Geophys. J Int.*, **172**(3), 1016-1032, doi:10.1111/j.1365-246X.2007.03685.x

Visser, K., Trampert, J., Lebedev, S., and Kennett, B. L. N., 2008a. Probability of radial anisotropy in the deep mantle, *Earth Planet. Sci. Lett.*, **270**, 241-250, doi:10.1016/j.epsl.2008.03.041

Wookey, J. & Barruol, G., 2002. Mid-mantle deformation inferred from seismic anisotropy, *Nature*, **415**, 777-780, doi:10.1038/415777a

Yao, H., 2015. A method for inversion of layered shear wavespeed azimuthal anisotropy from Rayleigh wave dispersion using the Neighborhood Algorithm, *Earthq. Sci.* **28**(1), 59-69, doi:10.1007/s11589-014-0108-6

Yao, H., Beghein, C., & van der Hilst, R.D., 2008. Surface-wave array tomography in SE Tibet from ambient seismic noise and two-station analysis: II Crust and upper mantle structure, *Geophys. J Int.*, **173**(1), 205-219, doi:10.1111/j.1365-246X.2007.03696.x

Yuan, K., & Beghein, C., 2013. Seismic anisotropy changes across upper mantle phase transitions, *Earth Planet. Sci. Lett.*, **374**, 132-144, doi:10.1016/j.epsl.2013.05.031

Yuan, K., & Beghein, C., 2014. Three-dimensional variations in Love and Rayleigh wave azimuthal anisotropy for the upper 800 km of the mantle, *J. geophys. Res.*, **119**(4), 3232-3255, doi:10.1002/2013JB010853

Table 1. Average χ^2 misfit for the model obtained by regularized inversion and for the mean NA model.

Model	$n = 0 - 6$	$n = 0$	$n = 1$	$n = 2$	$n = 3$	$n = 4$	$n = 5$	$n = 6$
YB17SVaniSVD	0.04	0.02	0.023	0.04	0.07	0.04	0.07	0.07
Mean NA model	0.17	0.56	0.18	0.20	0.19	0.14	0.24	0.33

Table 2. Average variance reduction for the model obtained by regularized inversion and for the mean NA model.

Model	$n = 0 - 6$	$n = 0$	$n = 1$	$n = 2$	$n = 3$	$n = 4$	$n = 5$	$n = 6$
YB17SVaniSVD	0.94	0.95	0.93	0.89	0.80	0.77	0.66	0.45
Mean NA model	0.79	0.88	0.68	0.71	0.67	0.50	0.40	0.20

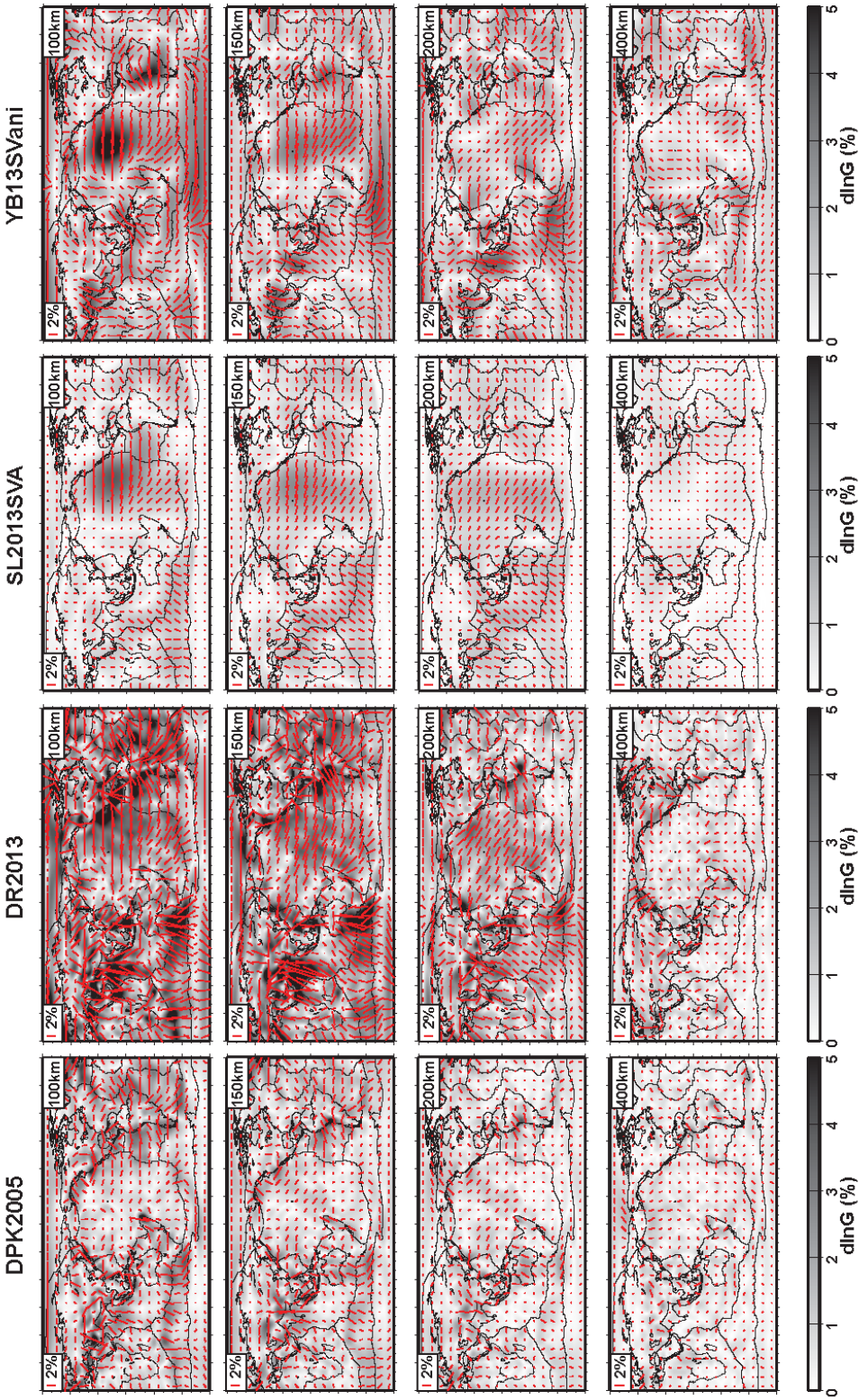

Figure 1. Azimuthal anisotropy models in the top 400 km of the mantle from previous studies: DPK2005 (Debayle et al. 2005), DR2013 (Debayle & Ricard 2013), SL2013SVA (Becker et al. 2014), and YB13SVani (Yuan & Beghein 2013).

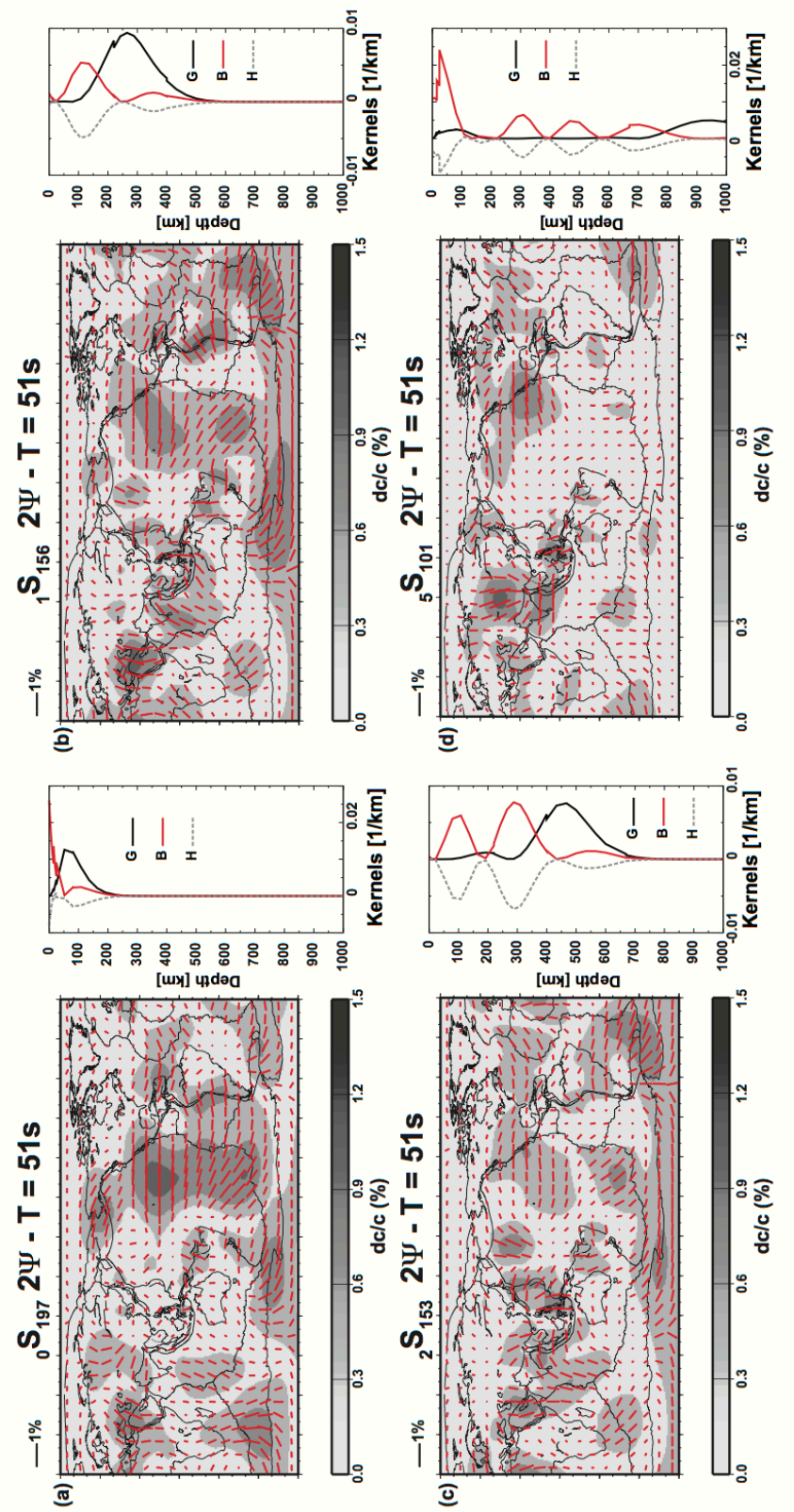

Figure 2. 2Ψ azimuthally anisotropic Rayleigh wave phase velocity maps (Visser et al. 2008b) at 51 s period for the fundamental mode (a), the first (b), second (c), and fifth (d) overtone, and associated partial derivatives. The sensitivity kernels were calculated using reference model PREM (Dziewonski & Anderson 1981) for relative perturbations in parameters G, B, and H.

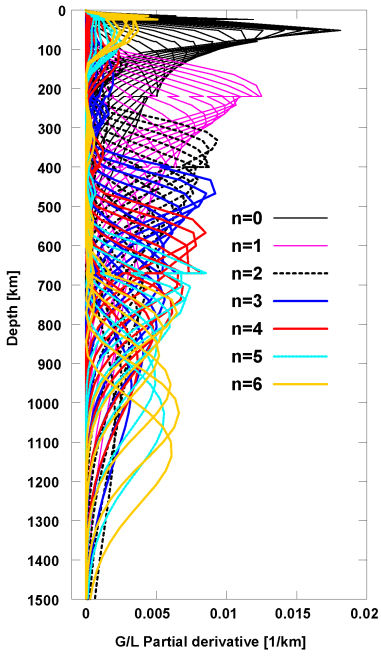

Figure 3. Phase velocity partial derivatives for relative perturbations in vertically polarized shear-wave azimuthal anisotropy. These sensitivity kernels were calculated using model PREM for the fundamental modes and first six higher modes employed in this study.

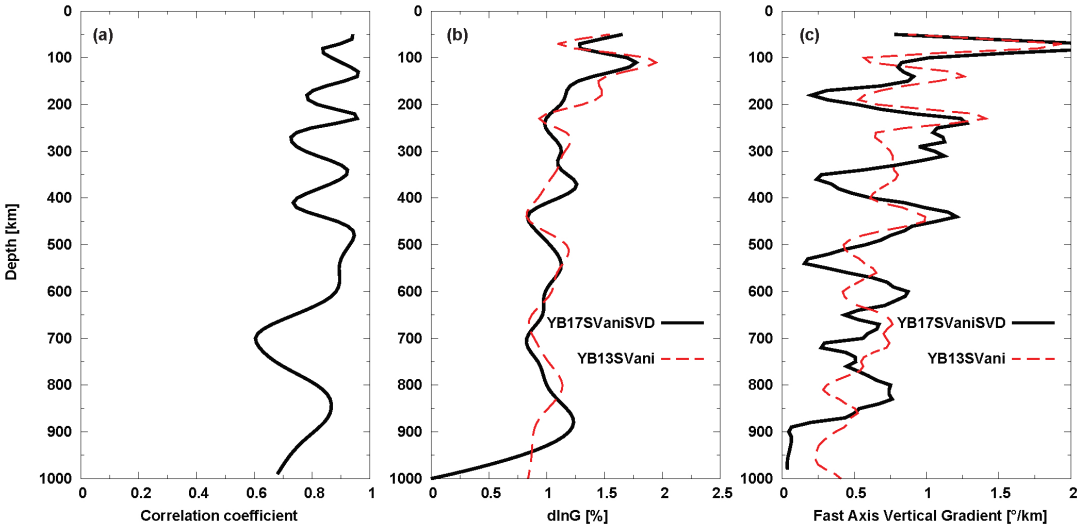

Figure 4. (a) Correlation coefficient between new model YB17SVaniSVD and model YB13SVani (Yuan & Beghein 2013); root mean square amplitude (b) and gradient of the fast axes direction (c) of models YB17SVaniSVD and YB13SVani.

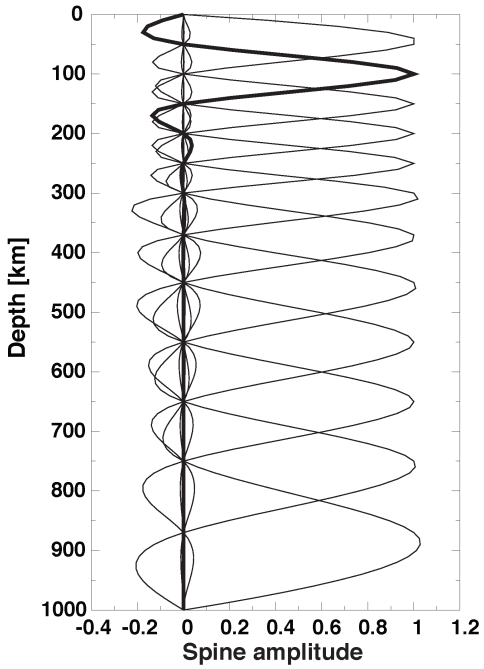

Figure 5. Splines functions employed (a) to parameterize $G_c(r)$ and $G_s(r)$ and (b) to parameterize $H_c(r)$, $H_s(r)$, $B_c(r)$, and $B_s(r)$.

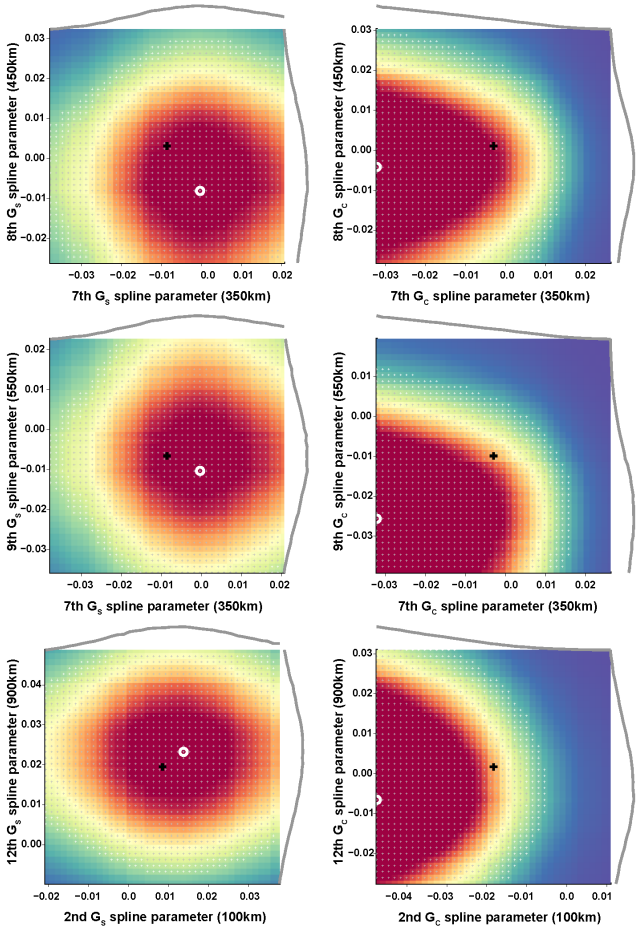

Figure 6. Examples of 1-D and 2-D marginal distributions at the grid cell located at -55° longitude and -60° latitude. The 1-D marginals are represented by the thick grey curves. The black cross indicates the location of the regularized inversion result around which the model space search was performed. The white circle is for the peak of the 2-D PPDF.

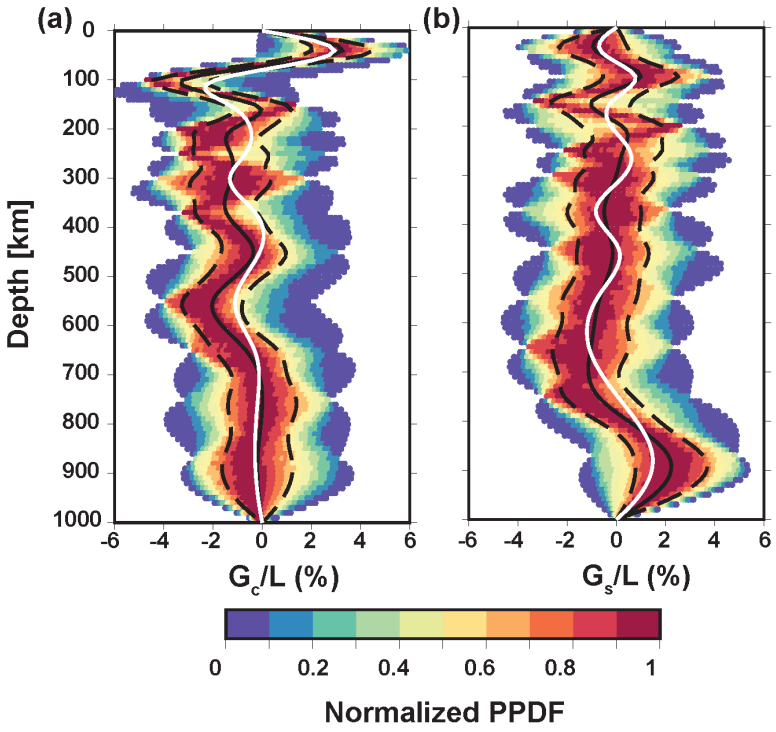

Figure 7. Example of normalized PPDFs for (a) G_c/L, and (b) G_s/L at $-55°$ longitude and $-60°$ latitude. L is the Love (1927) elastic coefficient that controls the speed of vertically polarized shear waves. The solid black lines represent the mean values of the distributions, the dashed black lines represent one standard deviation, and the solid white line is from model YB17SVaniSVD at the same location.

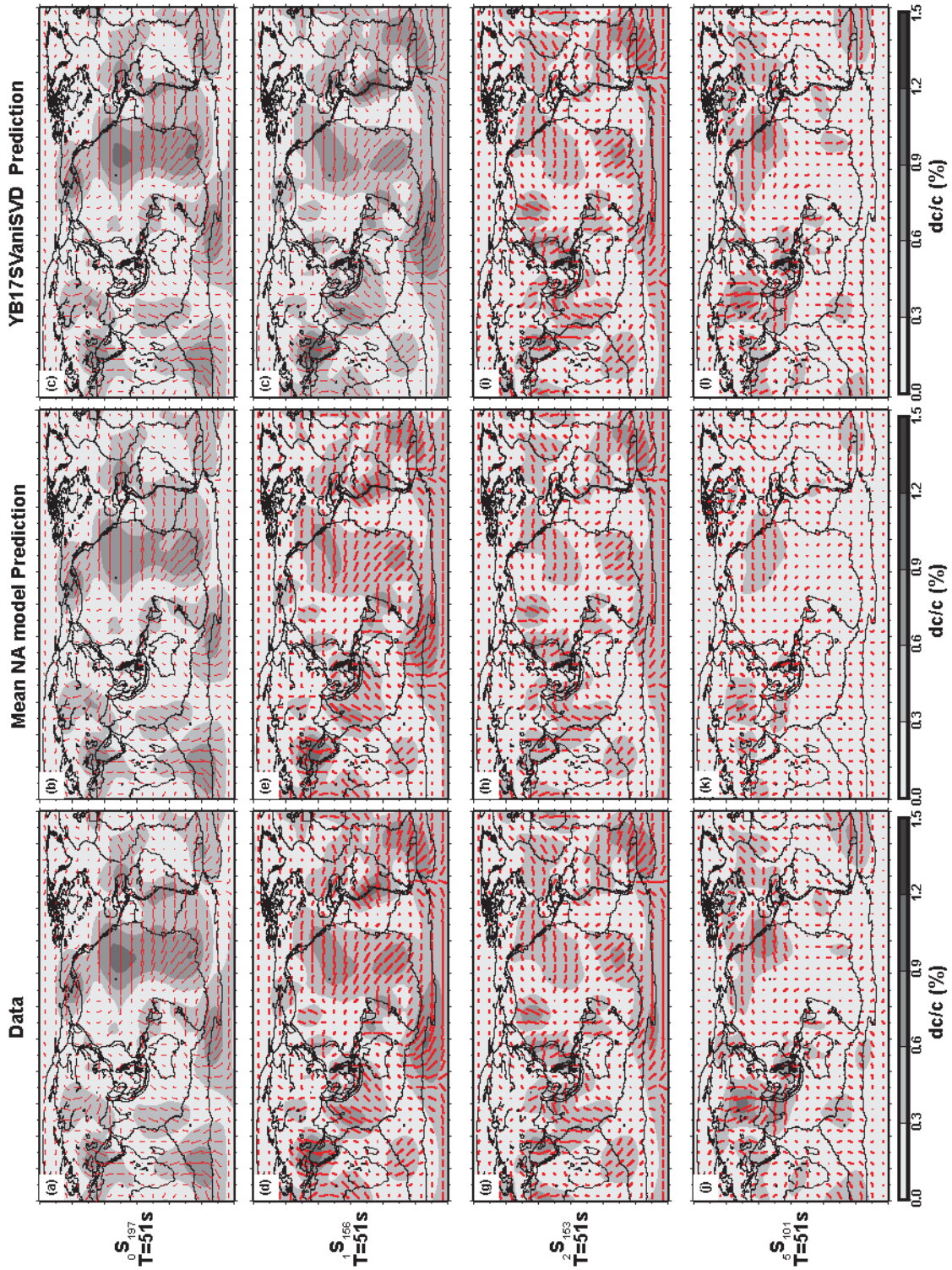

Figure 8. Phase velocity maps measured by Visser et al. (2008b) (left) compared to predictions from the mean NA model (middle) and from the model obtained by singular value decomposition (right) for the 51s Rayleigh wave fundamental mode ((a)-(c)), first overtone ((d)-(f)), second overtone ((g)-(i)), and fifth ((j)-(l)) overtone.

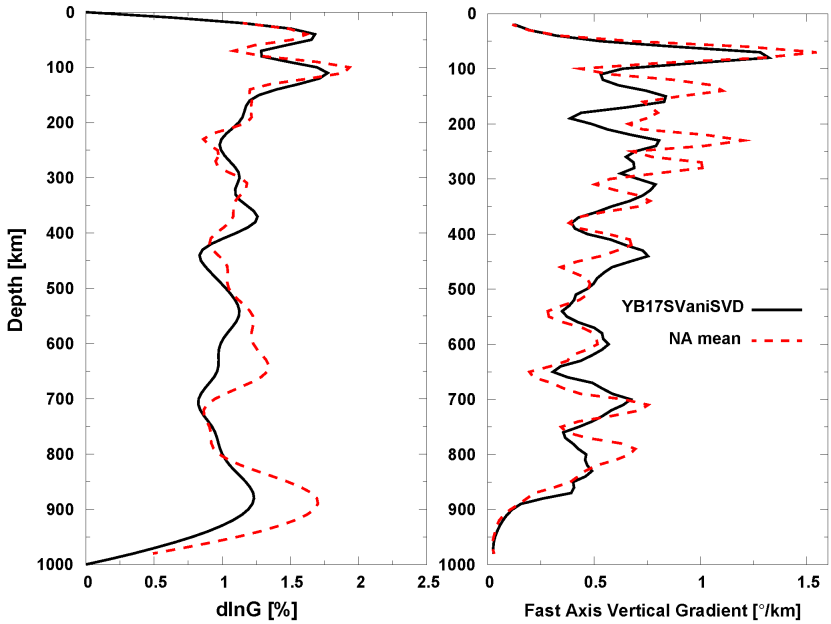

Figure 9. 1-D average model amplitude (left) and gradient of the fast axis direction (right) calculated from the mean G_s and mean G_c distributions. Model YB17SVaniSVD is shown by the black curves for comparison.

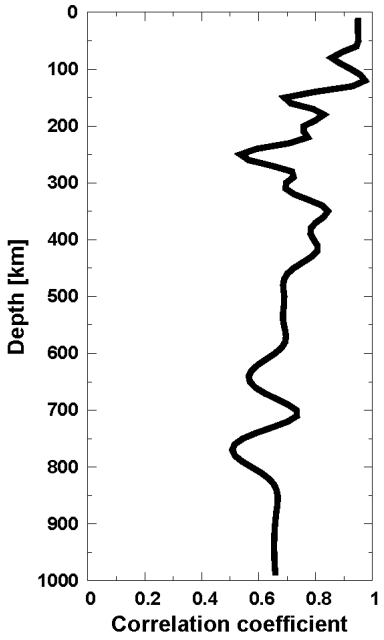

Figure 10. Correlation between YB17SVaniSVD and the mean NA model obtained from the mean $G_s(r)$ and mean $G_c(r)$ distributions.

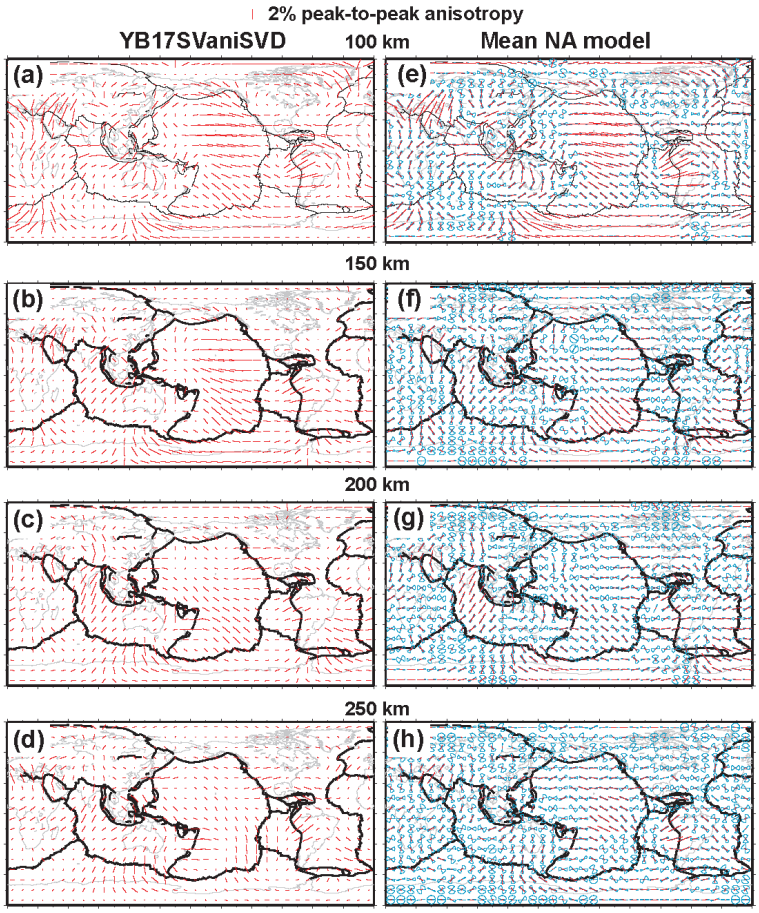

Figure 11. Model YB17SVaniSVD (a-d) obtained by regularized inversion and mean mantle model (e-h) obtained using the NA for the uppermost mantle. The model is shown in red in all panels, and fast axes direction standard deviation obtained from the NA is shown in blue in panels (e)-(h). The anisotropy amplitude is proportional to the length of the red bars. Plate boundaries are shown by black lines, and continents are delimited by thin grey lines.

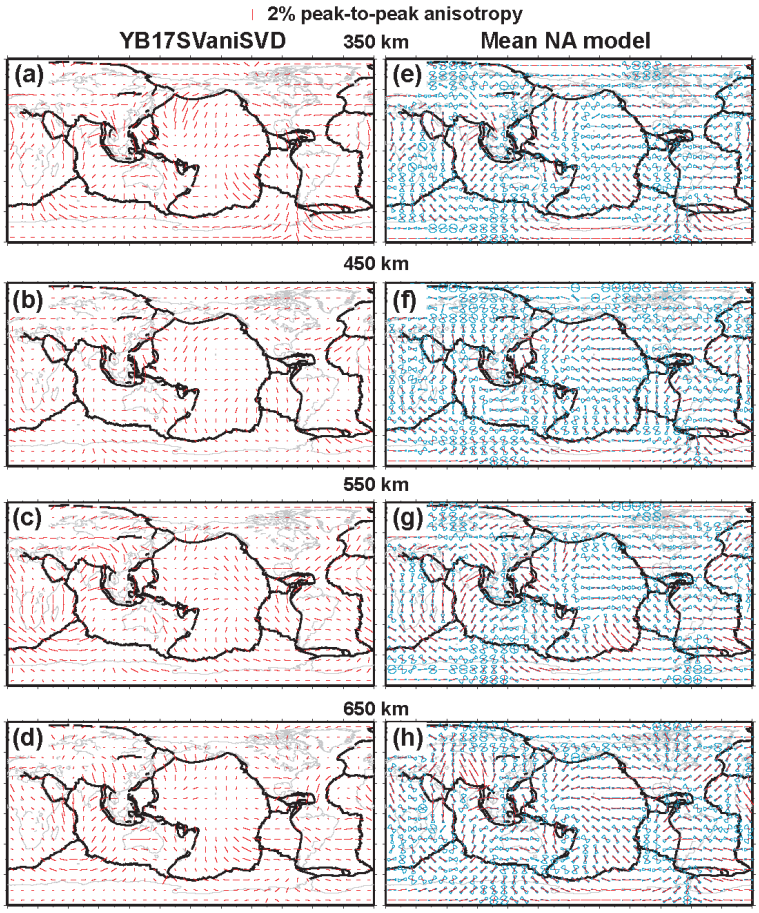

Figure 12. Model YB17SVaniSVD (a-d) obtained by regularized inversion and mean mantle model obtained using the NA (e-h) for the deep upper mantle. The model is shown in red in all panels, and fast axes direction standard deviation obtained from the NA is shown in blue in panels (e)-(h). The anisotropy amplitude is proportional to the length of the red bars. Plate boundaries are shown by black lines, and continents are delimited by thin grey lines.

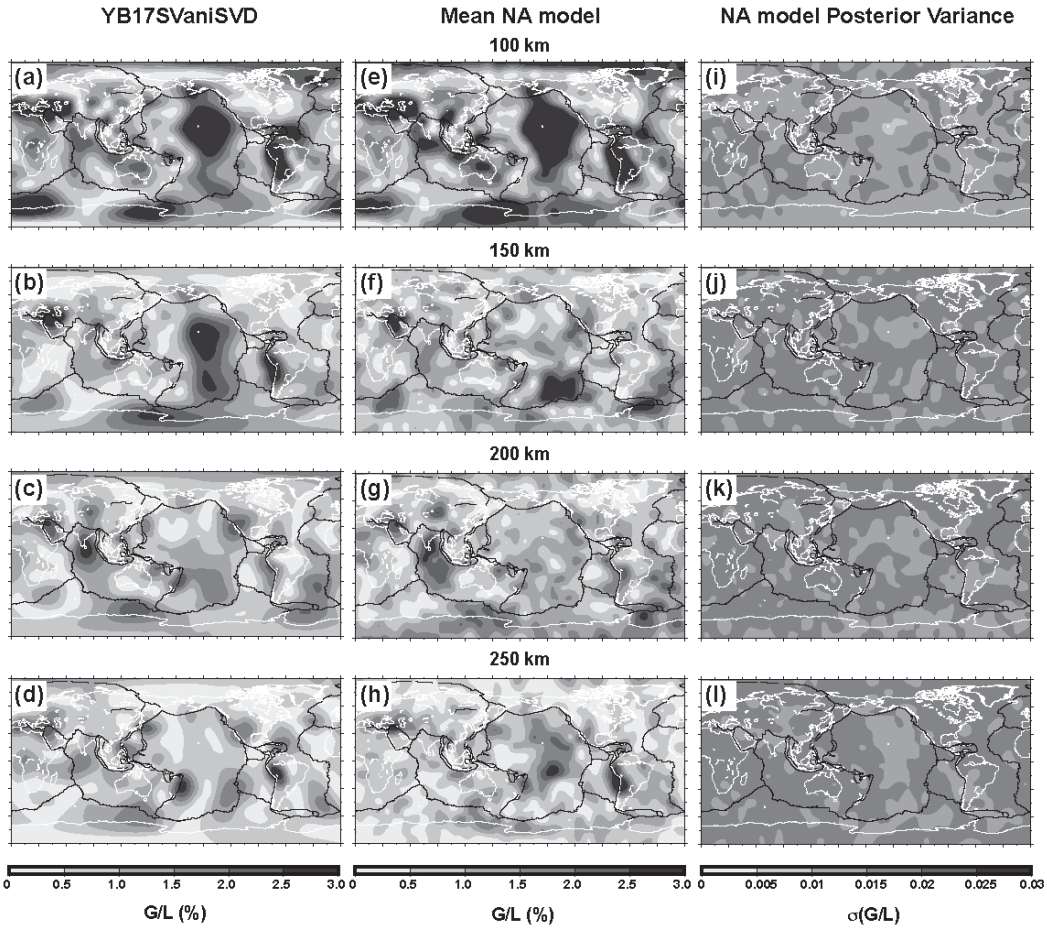

Figure 13. Amplitude of model YB17SVaniSVD (a-d), of the mean mantle model obtained using the NA (e-h) for the uppermost mantle, and mean model amplitude standard deviation (i-l). Plate boundaries are shown by black lines, and continents are delimited by thin white lines.

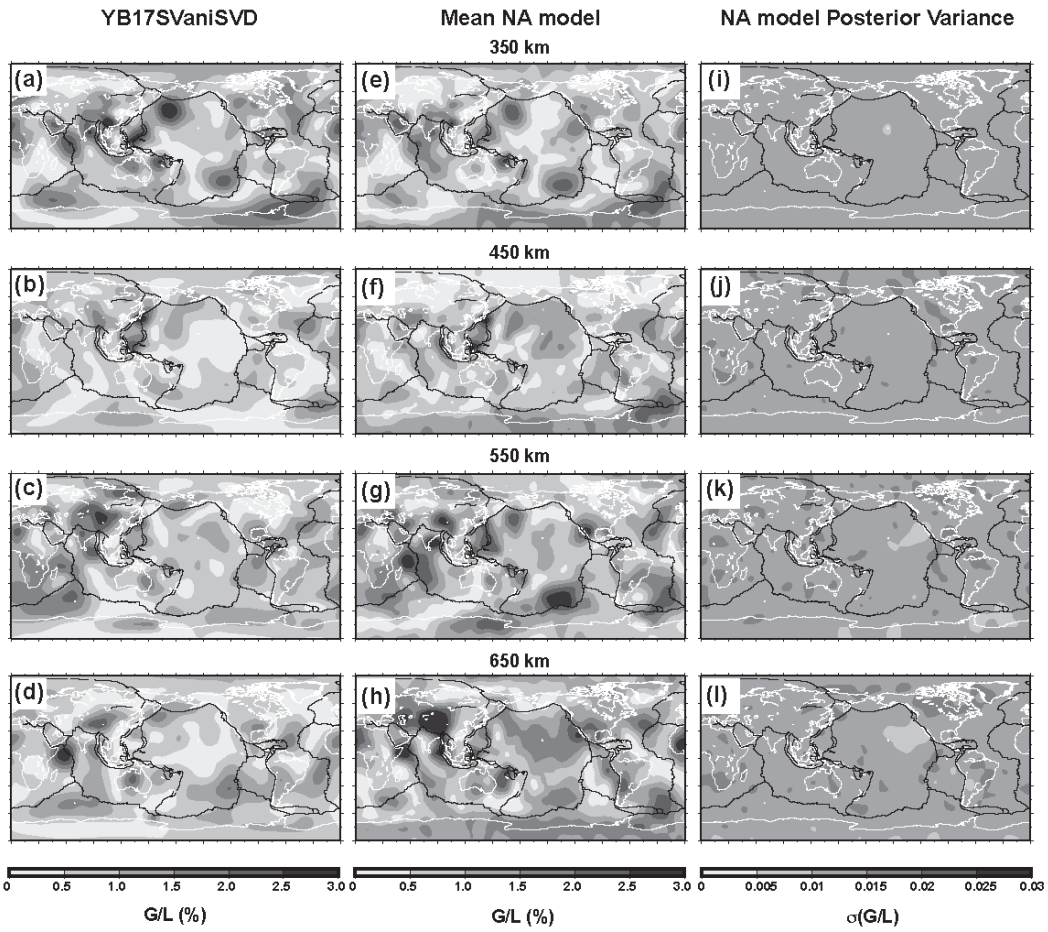

Figure 14. Amplitude of model YB17SVaniSVD (a-d), of the mean mantle model obtained using the NA (e-h) for the deep upper mantle, and mean model amplitude standard deviation (i-l). Plate boundaries are shown by black lines, and continents are delimited by thin white lines.

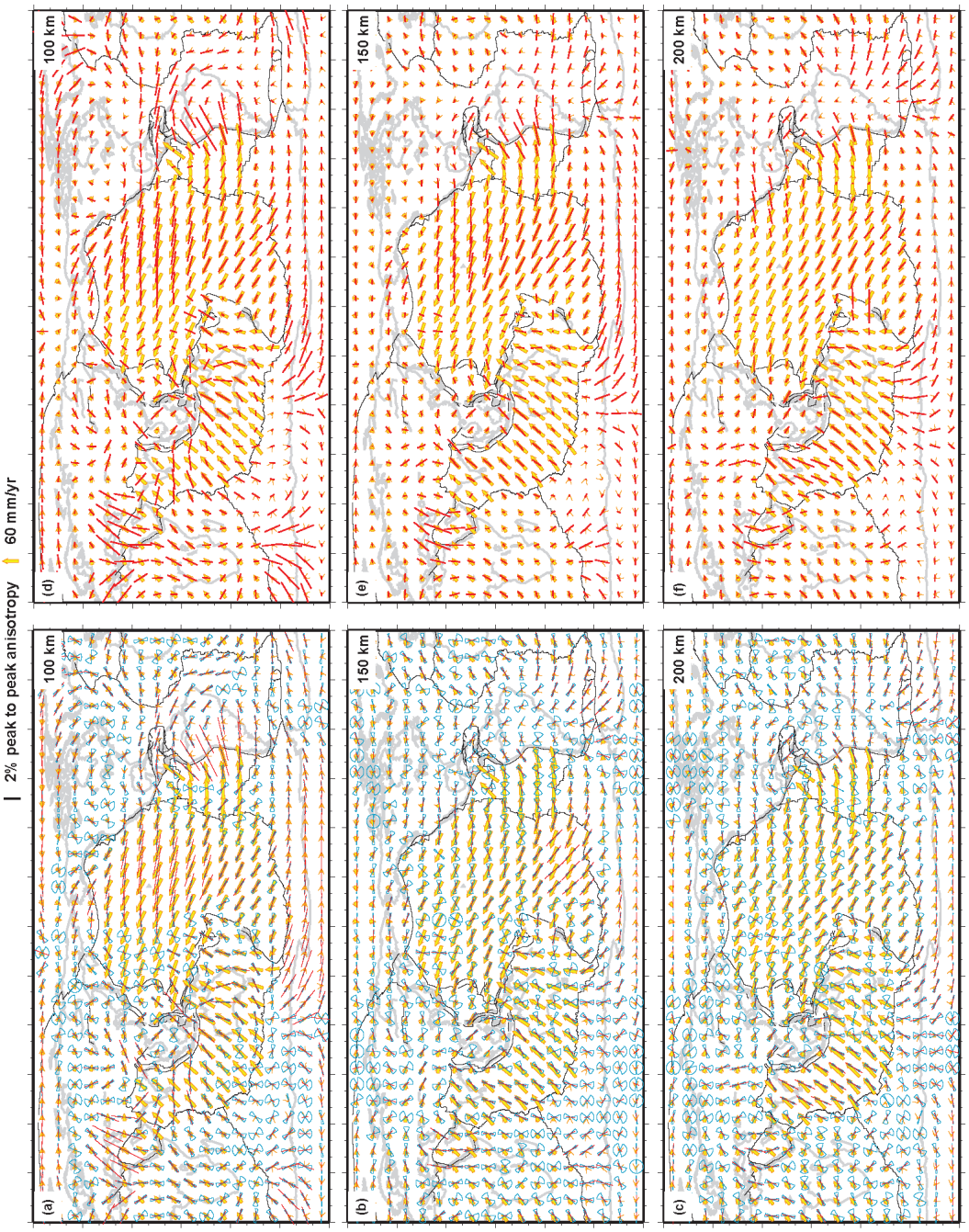

Figure 15. Comparison between the APM directions (yellow arrows) and the fast seismic directions (red bars) for the mean NA model ((a)-(c)) and YB17SVaniSVD ((d)-(f)). The APM was calculated using the no-net rotation reference model NNR-NUVEL 1A (Gripp & Gordon 2002). The mean NA model fast direction is plotted with its standard deviation (blue). Plate boundaries are shown by black lines, and continents are delimited by grey lines.

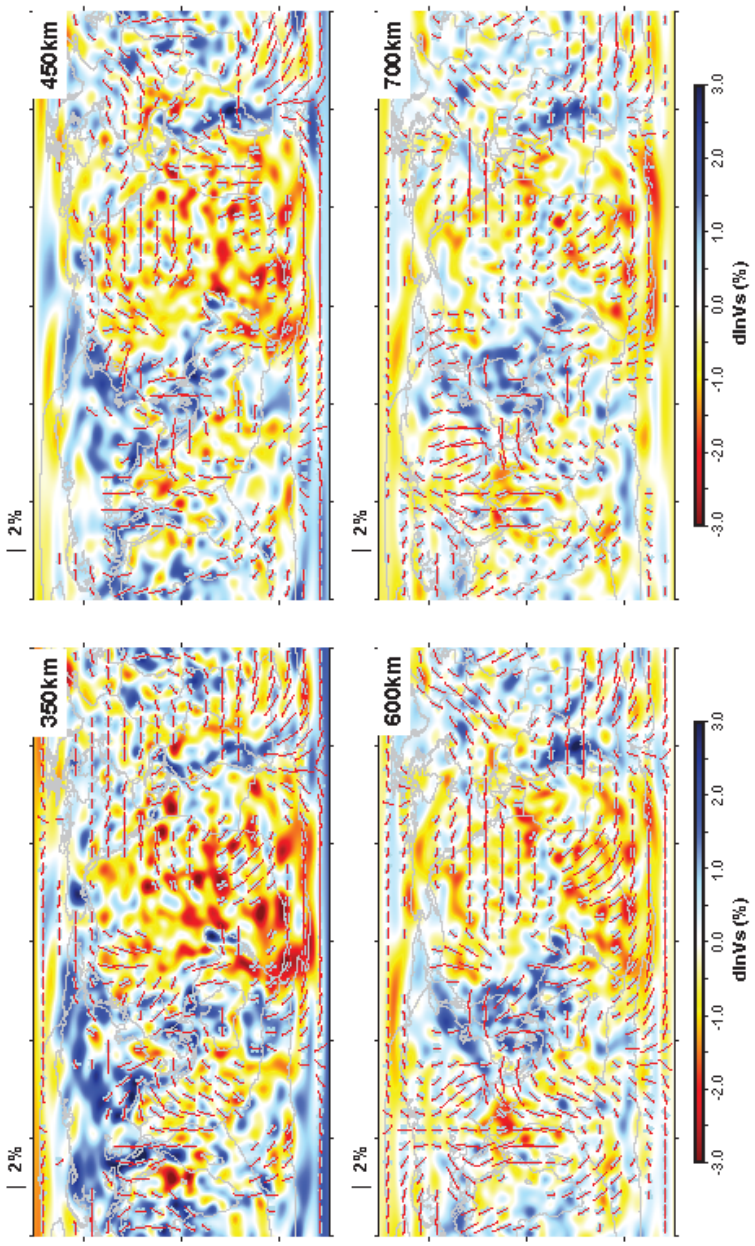

Figure 16. Fast seismic direction in locations where the uncertainty is lower than $45°$. The color background represents isotropic velocity model SEMUCB (French & Romanowicz 2014).

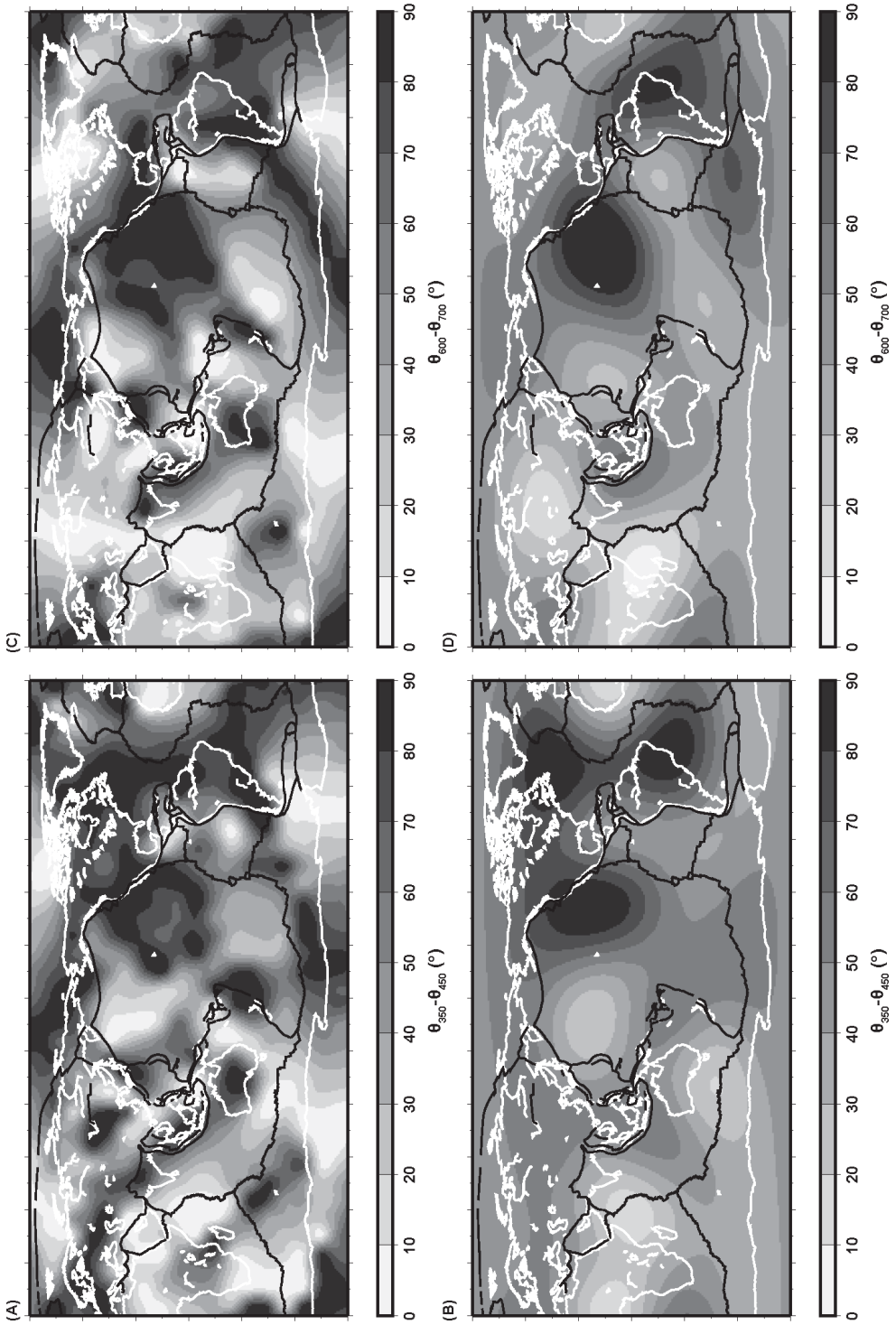

Figure 17. Difference between mean fast axis Θ_m across the 410- and 670- discontinuities. (A) and (B) represent the difference between the fast direction at 350 km and 450 km depth, and (C) and (D) is the difference between fast directions at 600 km and 700 km. (A) and (C) were determined at every grid cell we used to parametrize Earth's surface. (B) and (D) were obtained by filtering (A) and (C) up to spherical harmonic degree 5. Plate boundaries are shown by black lines, and continents are delimited by white lines.

Supplementary Material - A Bayesian Method to Quantify Azimuthal Anisotropy Model Uncertainties: Application to Global Azimuthal Anisotropy in the Upper Mantle and Transition Zone

Figure S1 shows that whether the NA searches for G or for G, B, and H, the results for G are identical. We can therefore neglect the less well resolved B and H parameters safely.

Figure S2 compares synthetic tests made using the NA when the model is sampled around the SVD inversion results and around PREM. It shows that whether the model space is sampled around zero or around the SVD model, the peak of the resulting PPDFs are close to the input model and in the few cases where they do not match (e.g. G_3 and G_4 in case 1), the input model is within the uncertainties one would determine from the PPDFs.

Figure S3 displays NA results for real data inversion using the Visser et al. (2008) dataset and searching the model space for G values (neglecting B and H). In case 1, the model is sampled around the SVD inversion results and in case 2 around PREM. It demonstrates that the models obtained are in agreement with one another, independently of the prior boundaries of the model space, provided these bounds are large enough.

Figure S4 compares uncertainties calculated using the NA and using the covariance matrix of the model obtained by regularized inversion. It demonstrates that posterior model errors can be underestimated by regularized inversion methods.

Figure S5 displays synthetic tests that show that the model corresponding to the mean of the reconstructed dlnG or Θ distributions, hereafter referred to as $\mathrm{dlnG_{mean}}$ and Θ_{mean}, can differ strongly from the model built with the mean of the individual $\mathrm{dlnG_c}$ and $\mathrm{dlnG_s}$ distributions (referred to as $\mathrm{dlnG_{c,mean}}$ and $\mathrm{dlnG_{s,mean}}$). In other words:

$$\mathrm{dlnG_{mean}} \neq \sqrt{\mathrm{dlnG_{c,mean}}^{\,2} + \mathrm{dlnG_{s,mean}}^{\,2}} \text{ and}$$

$$\Theta_{\mathrm{mean}} \neq \frac{1}{2} arctan\left(\mathrm{dlnG_{s,mean}} / \mathrm{dlnG_{c,mean}}\right)$$

This is somewhat counter-intuitive since these synthetic tests assume Gaussian distributions. The model corresponding to the mean of the G_c^i and G_s^i PPDFs is thus the model that best explains the data, and one might therefore expect that same model to correspond to $\mathrm{dlnG_{mean}}$ and Θ_{mean}. Our synthetic examples show that the two models differ when the $\mathrm{dlnG_c}$ and $\mathrm{dlnG_s}$ distributions are both centered on zero or with peaks close to zero, i.e. the parameters are not well resolved (Figure S5(f)), or when one the distributions is highly skewed (Figure S5(g) and (h)). We also see that the PPDFs for Θ are even more sensitive than dlnG to the shape of the combined $\mathrm{dlnG_c}$ and $\mathrm{dlnG_s}$ PPDFs. The PPDFs for Θ can be highly skewed (Figure S5(b)), or have multiple peaks (Figure S5(c)-(f)).

Figure S6 represents the map of the mean fast direction Θ_{mean} and its uncertainty at 150km depth calculated by resampling the $\mathrm{dlnG_c}$ and $\mathrm{dlnG_s}$ PPDFs. The map of the model obtained from the mean G_c and mean G_s is also shown for comparison. The resulting Θ PPDFs have a mean that is far from the fast direction calculated directly from the mean G_c and mean G_s. This results in a map of azimuthal anisotropy that is difficult to interpret and compare with other models, which is why we abandoned this method to calculate errors on the fast axes.

Figure S7 is an example of $\mathrm{dlnG_c}$ and $\mathrm{dlnG_s}$ PPDFs and resulting dlnG and Θ PPDF after drawing random samples from the G_c and G_s distributions. This was determined for the second spline parameters using real data.

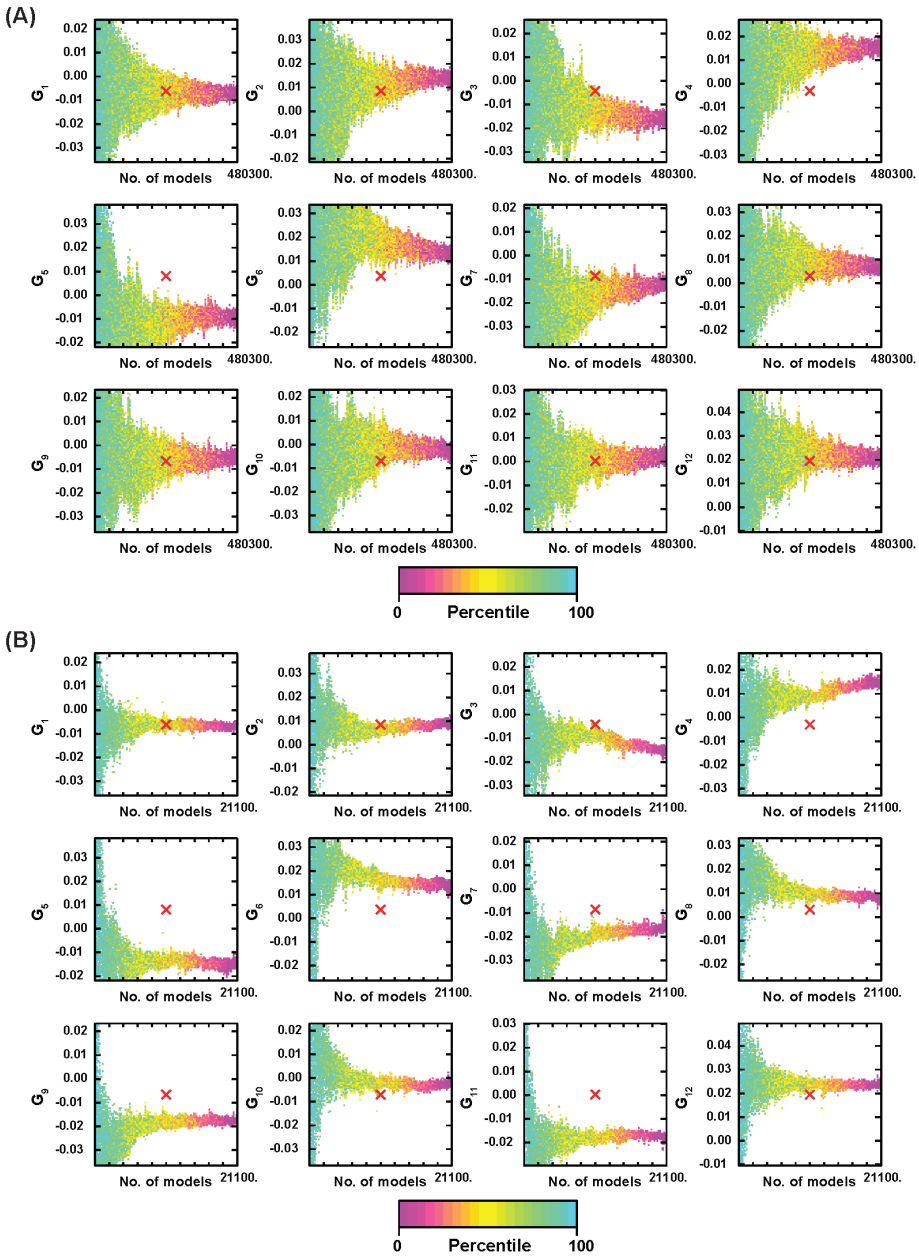

Fig. S1: Inversion using the NA of the Visser et al. (2008) dataset at a grid cell located at -25° lat and 305° lon. (A) is for a model space search for $dlnG_c$, $dlnB_c$, and $dlnH_c$ using 12 cubic spline functions for $dlnG_c$. $dlnH_c$ and $dlnB_c$ were parameterized each with 6 cubic spline functions. We chose to use a coarser parameterization for these other parameters because are poorly resolved due to the similarity of their partial derivatives. (B) is for a model space search for $dlnG_c$ only using the same 12 splines as in (A). In each case, the model space search was performed around model YB17SVaniSVD, indicated by the red cross, allowing for perturbations between -0.03 and 0.03. The spline parameters are displayed as a function of the number of models generated. We labeled them as G_i (1=1,…,12) instead of $dlnG_{c,i}$ for simplicity.

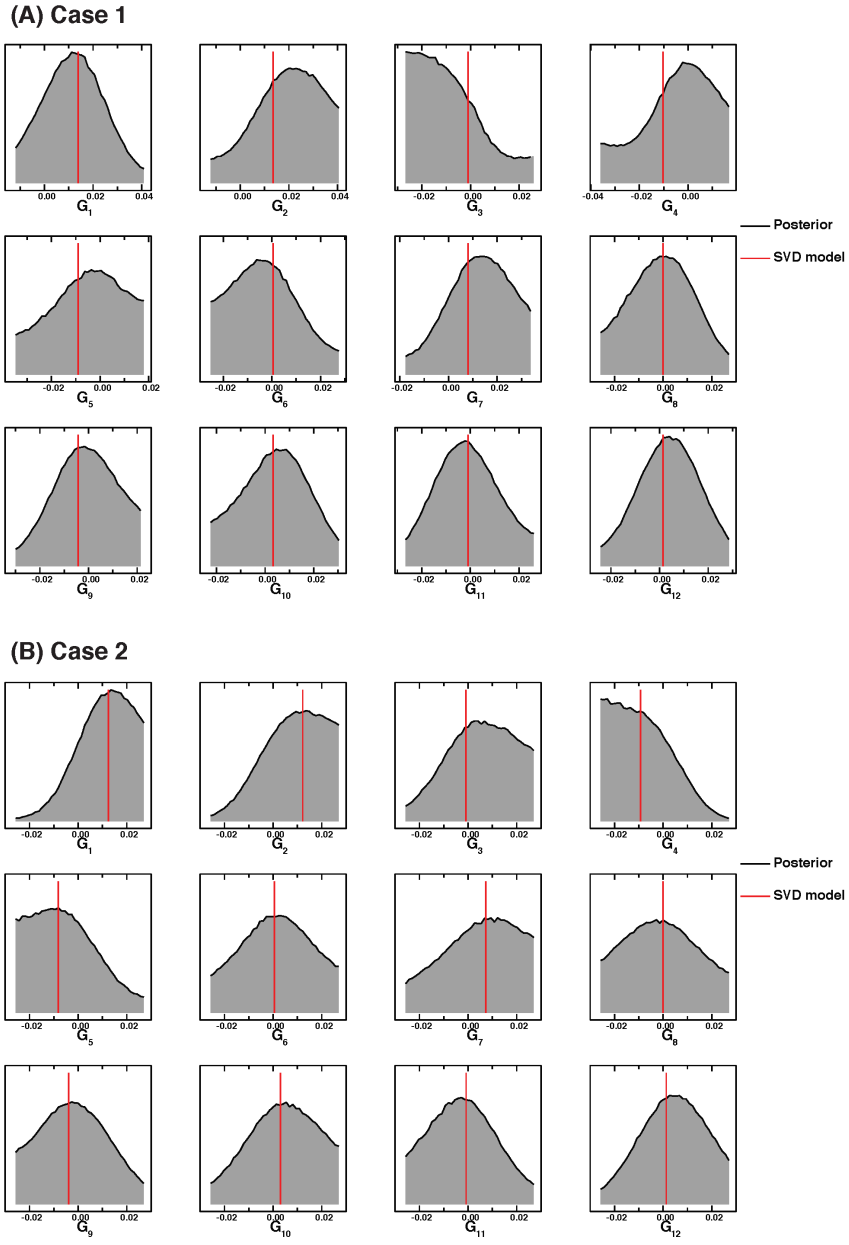

Fig. S2: Synthetic tests comparing NA results when the model is sampled around the SVD inversion results (case 1) and around PREM (case 2, zero azimuthal anisotropy). Note that the axes labels in case 1 and case 2 are different. The model employed to calculate the synthetic data was model YB17SVaniSVD, denoted by the red bar.

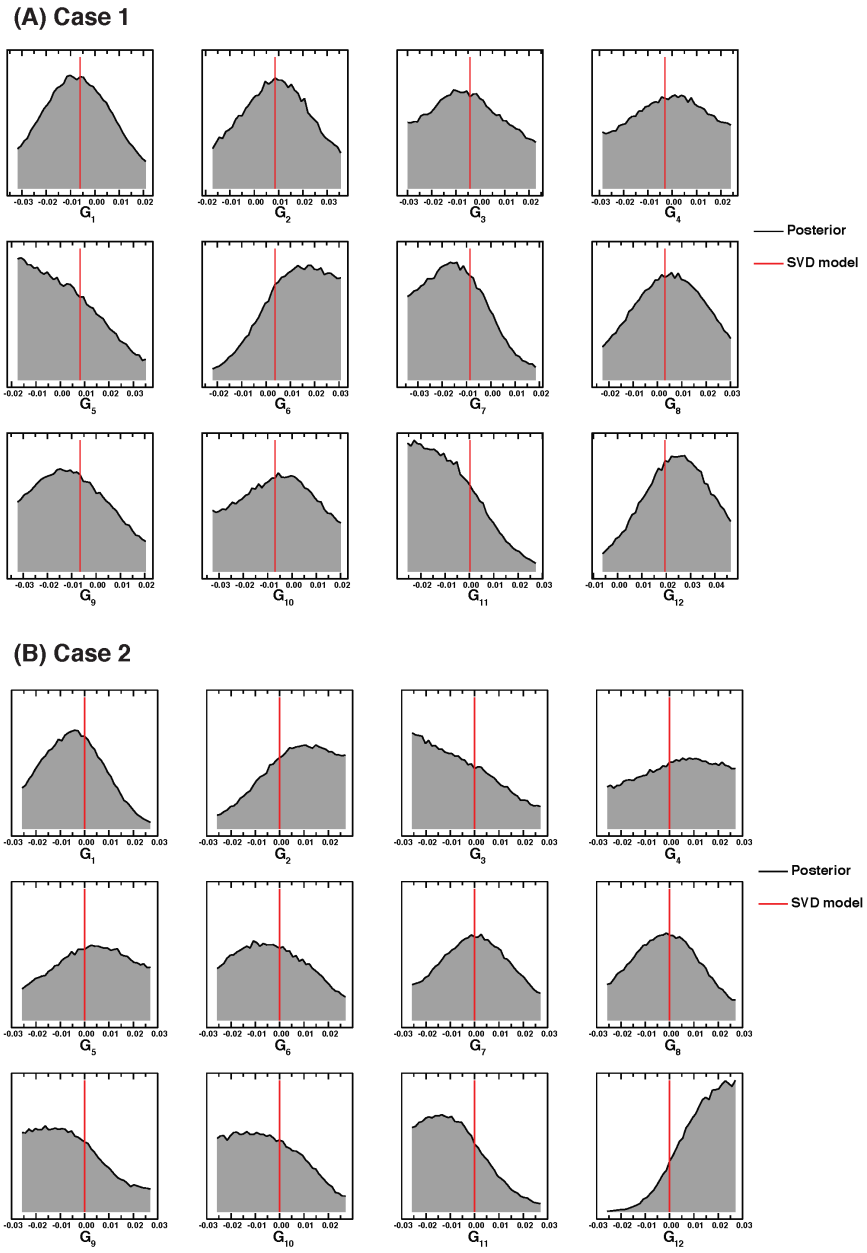

Fig. S3: NA results using the Visser et al. (2008) dataset and searching the model space for G values (neglecting B and H). Case 1 corresponds to searching the mode space around YB17SVaniSVD (represented by the red line) and case 2 corresponds to searching around PREM (zero azimuthal anisotropy). Note that the axes labels in case 1 and case 2 are different.

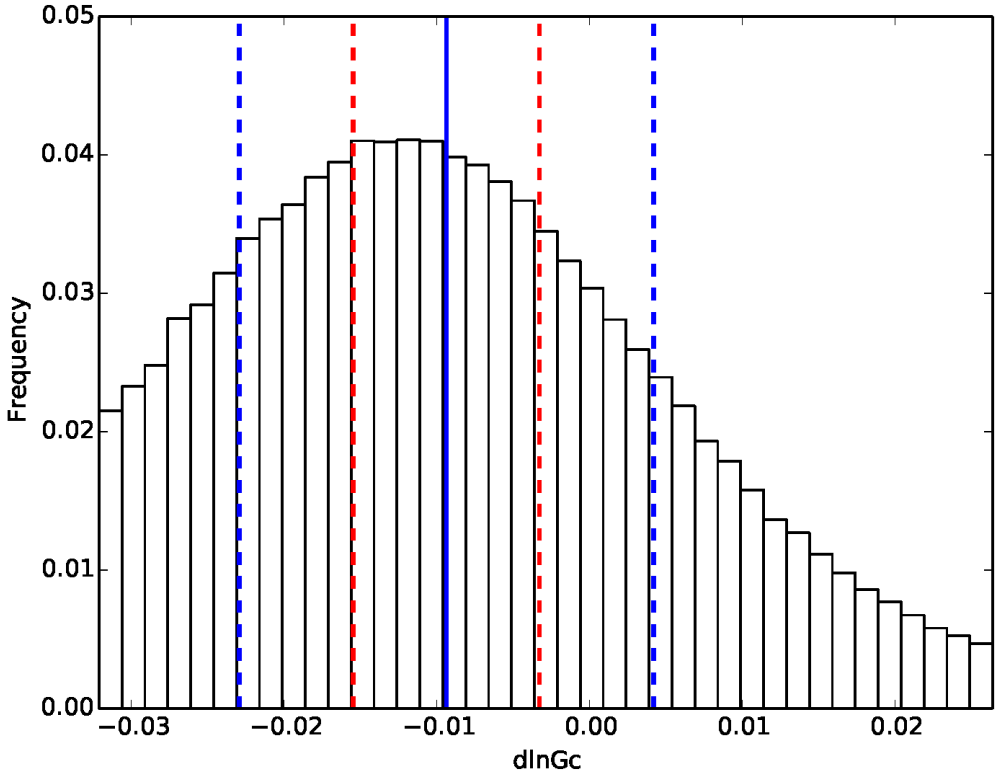

Fig. S4: Comparison of uncertainties calculated using the standard deviation (dashed blue lines) of the PPDF obtained from NA and using the covariance matrix of the model obtained by regularized inversion (dashed red line). The solid blue line corresponds to the mean model. The data point corresponding to this PPDF was located at 175° longitude and -85° latitude.

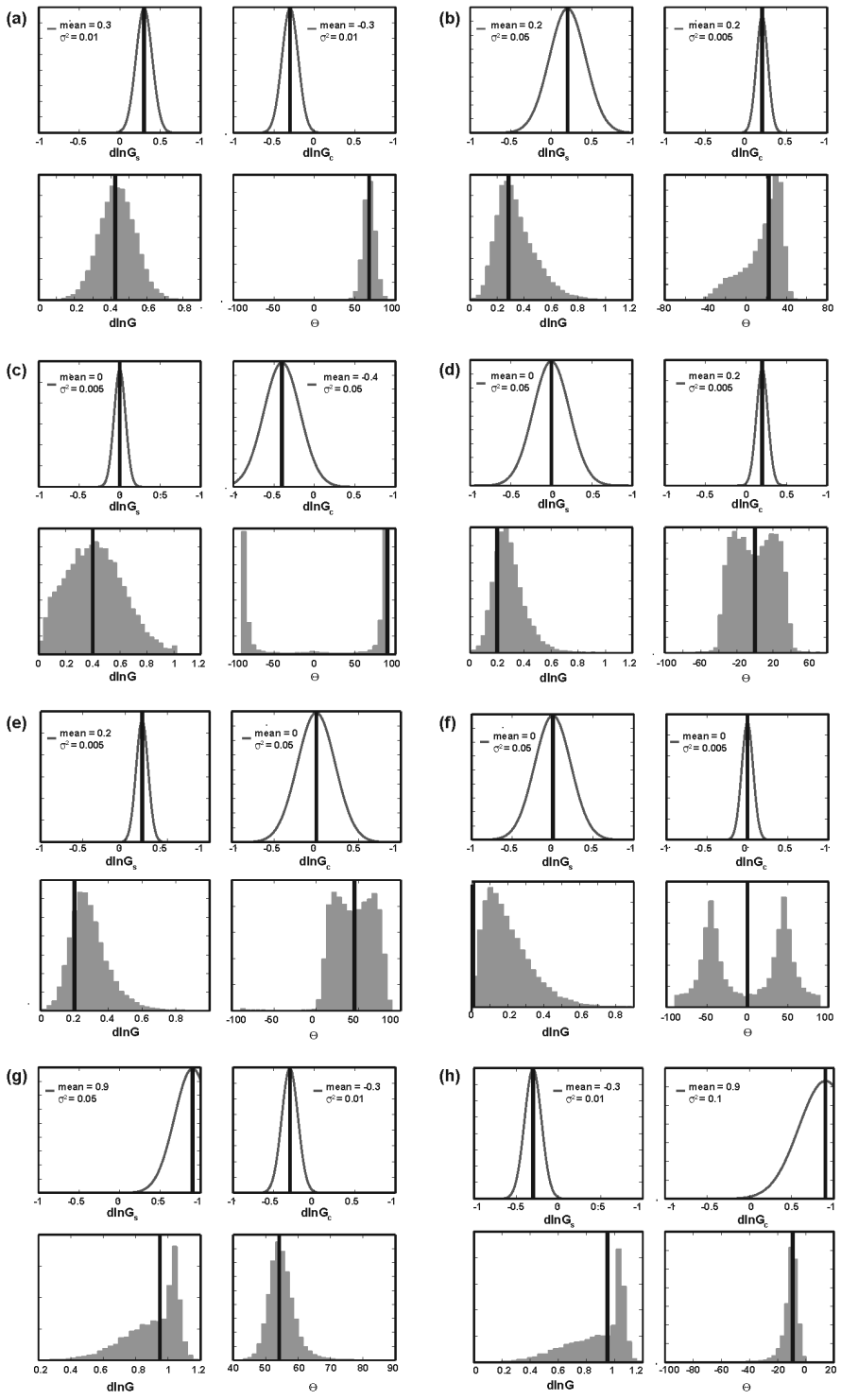

Fig. S5: Synthetic examples of resampled dlnGc and dlnGs PPDFs to calculate dlnG and Theta distributions. Each of the six panels corresponds to different $dlnG_c$ and $dlnG_s$ distributions, with different means and variances as indicated in the legends. In each panel, the black vertical line in the $dlnG_c$ and $dlnG_s$ indicates the mean of the $dlnG_c$ and $dlnG_s$ PPDFs. The black vertical line in the reconstructed dlnG and Θ distributions indicates the value of dlnG and Θ calculated from the mean of the $dlnG_c$ and $dlnG_s$ distributions.

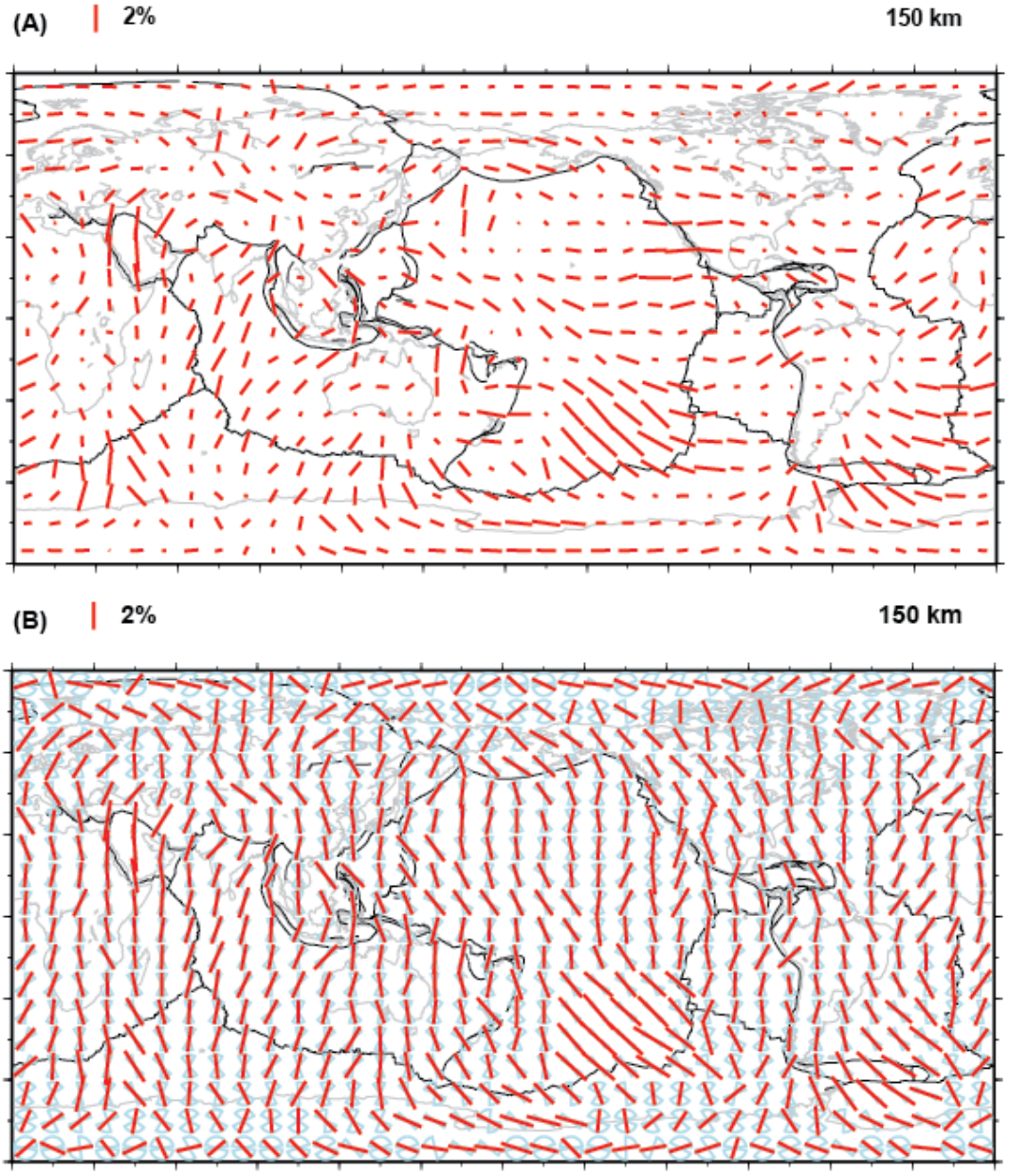

Fig. S6: (A) Map of mean fast direction calculated from the mean G_c and G_s and (B) map of the mean model and its standard deviation obtained by drawing random samples from the G_c and G_s PPDFs. Both were calculated at 150km depth. Plate boundaries are represented by thin black lines and continents are in grey.

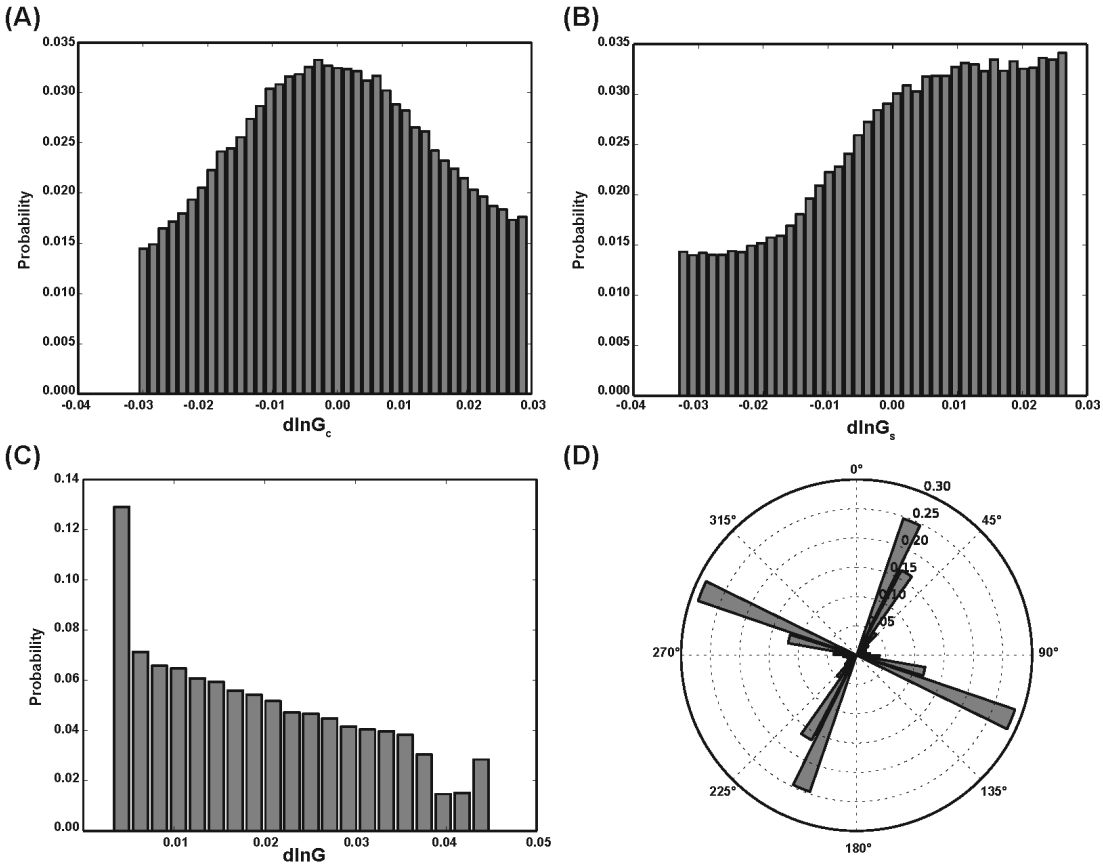

Fig. S7: (A) and (B) are PPDFs for $dlnG_c$ and $dlnG_s$ obtained from the NA using the Visser et al. (2008) data and the NA. (C) and (D) are the reconstructed dlnG and Θ PPDFs after drawing random samples from the $dlnG_c$ and $dlnG_s$ PPDFs.

References:

Visser, K., Trampert, J., and Kennett, B. L. N., 2008. Global anisotropic phase velocity maps for higher mode Love and Rayleigh waves, *Geophys. J Int*., **172** (3), 1016-1032, doi:10.1111/j.1365-246X.2007.03685.x

Response to Reviewers

A point-by-point response to the reviewers comments can be found below in blue and bold font.

Reviewer: 1

Comments to the Author(s)

This is a retyping of the review that I previously stupidly typed into the interface and lost when the Scholar One site went down, so I hope it comes across okay. This is an interesting and important study using the neighbourhood algorithm in order to quantify uncertainties in a global inversion for anisotropic velocity based on Rayleigh wave phase velocity maps. I grade this as accept with major revision, although I could see it as moderate revision depending upon the opinion of the editor.

The rest of the review proceeds more or less in order through the manuscript, mixing minor edits and substantive criticism:

[Q1] Page 3, line 41: Extra parenthesis in the reference list needs to be removed

The extra bracket has been removed.

[Q2] Page 5, section 2: I assume this is an identical dataset as the one used to create YB13SVani. If so, this should be stated explicitly, and if not, you should describe how it differs.

Yes, this is the same dataset that generated YB13SVani. We now explicitly say so in the first sentence of section 2.

[Q3] Page 5, line 56: You reference equation 1 well before defining it in the text. If you need to reference it here, you should define it here, or wait to reference it until section 3.

We thank the reviewer for noticing this. To avoid this problem, we combined section 2 and what was section 3.1 into one section (new section 2).

[Q4] Page 6, last sentence of section 2: awkward sentence structure, and unclear what you're trying to say here.

We removed this sentence.

[Q5] Page 7, line 34: typo “doe snot” should be “does not” unless you mean to refer to female deer mucus!

Change “doe snot” to “dose not”.

[Q6] Page 7, line 33: you reference how the uncertainty analysis does not account for uncertainties stemming from non-uniform ray path coverage etc. Either here, or somewhere else, you need to explicitly say how your analysis does account for uncertainties in the input phase velocity maps. Presumably, you account for this in some fashion by including the variance of the estimated phase velocity dispersion at each pixel in the misfit function used by the NA. But you need to explicitly state how this is included or if it is neglected entirely.

After reflection, we decided to change our cost function into a chi-misfit to account for the uncertainties in the input phase velocity maps. We ran our codes again with the new cost function (see equation (11) in section 3.3. of the revised manuscript).

[Q7] Page 8, line 20, you say you only look at uncertainty for Gc and Gs. This is fair, but I think it’s important to try to understand what impact your choice to allow B and H terms to vary has on your final results, as compared to either neglecting or scaling the terms. I would imagine that it would result in somewhat broader posterior probability distributions, and this potentially give you a more rigorous uncertainty estimate, but this is not necessarily obvious. Given that removing or scaling these terms results in half as many model parameters, it would seem feasible to run your approach with one or both of these options which would help quantify whether this choice leads to additional bias or uncertainty.

We thank the reviewer for this comment. We compared results run for G only and for G, B, and H and those are displayed in Fig. S1. This shows that parameter G converges toward the same value in each case. Since we decided to run the code again using the chi misfit instead of the variance reduction as we had initially done (see answer to Q6), and considering the resulting G model and uncertainties are not strongly affected by whether we invert for 1 or 3 parameters, we made the choice to rerun the inversions for G only. The results presented in the revised manuscript are for a G only inversion, i.e. assuming B=H=0.

We also demonstrated that the NA run for G only can successfully recover an input G model. The following figure shows an example of posterior probability density function (PPDF) for 12 G model parameters obtained from NA. Red bars represent the input G parameters, which are consistent with the maximum peaks of PPDFs.

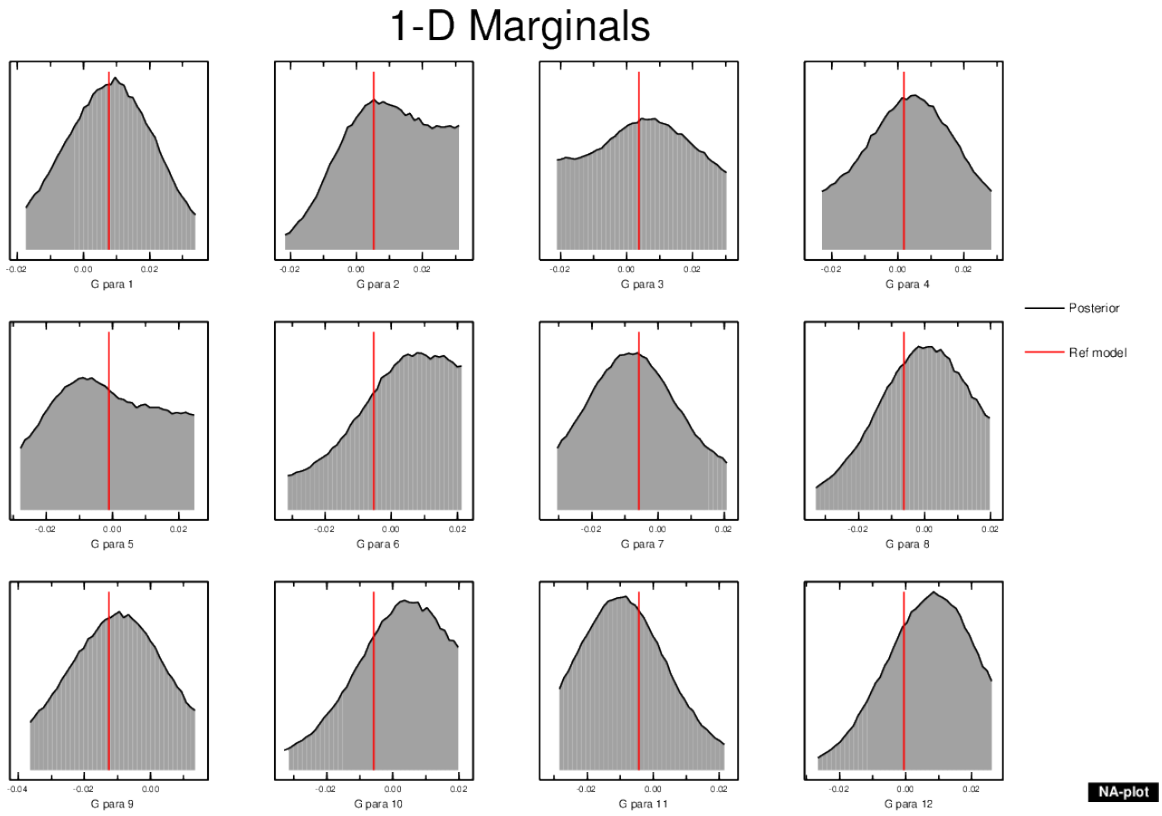

[Q8] Page 8, last sentence: You claim the new SVD model is "almost identical" to YB13SVani. What does this mean? I think a figure showing the rms profiles for the two models and their correlation as a function of depth would quantify this for the reader.

We added a new figure (Fig. 4) to show this.

[Q9] Page 10, around line 32: Why do you define your a priori limits around the values obtained in the SVD model? In some sense, this introduces a potential bias to your results, which may be reflected in some of the marginals in figures 5 and 6 which are peaked at the edge of the a priori range. Might it instead make more sense to do a broader range centered around 0? This may require more sampling of the model space, and it may not make any difference, but it seems a potentially problematic choice to do it the way you do here, when you then go on and make arguments based on whether the NA model is similar to the SVD model.

We agree with the reviewer that sampling the model space around a starting prior model can bias the results if the range within which we run the search is too narrow and if the model space is highly non-linear as the results may end up in a local minimum. The reason we chose to run the search around the SVD model in the previous version of this manuscript was because of the high computing cost of the NA. Searching around zero means searching a larger

model space and therefore much longer computations. In the present version of this manuscript, since we ran NA for G only, which dramatically decreased the size of the model space, we are able to present examples with a priori boundaries defined around the SVD model and around zero (Figs. S2 and S3).

We performed tests using the real data and synthetic data. In each case, we ran the NA around a solution obtained by SVD and around zero using model space boundaries wide enough to include the SVD solution. The results of these tests are shown here and in Fig. S2 for synthetics data and Fig. S3 for real data. From them, we conclude that for most model parameters, running the search around the SVD model or around zero does not significantly affect the solution: their PPDFs peak at the same location and the widths of the marginal are very similar. Note, also, that the posterior model uncertainties are large and not strongly affected by this choice either. Therefore, in an analysis of the models that accounts for model uncertainties, the boundaries of the model space are not going to affect the main conclusions, even if the peaks of the PPDFs depend on it, as long as the model space is large enough.

To answer the reviewer's comment regarding the fact that some parameters display PPDFs that peak at the edges of the model space, it would indeed seem natural to expand the range of the model space to avoid this. However, as noted in Beghein et al. (2002) and in Xing and Beghein (2015), it is important to keep in mind the existence of parameter trade-offs. While increasing the sampling range for one or multiple parameters may have the effect of reducing the minimum misfit somewhat, the trade- offs among the model parameters will cause the global minimum of other parameters to move as well. And they may, in turn, be directed towards the edge. Therefore, as long as there are trade-offs between model parameters, the model space cannot be surveyed completely guaranteeing that no solution lies at the edge of the model space. This is, fortunately, not a major problem because we can quantify these trade-offs with the NA. In addition, because the equations used in the present study rely on perturbation theory, we cannot increase the size of the model space we sample indefinitely to avoid violating the conditions of applicability of perturbation theory. The SVD model is a good starting point because it fits the data better than a model without azimuthal anisotropy (which corresponds to zero).

[Q10] Page 10, line 37: typo misspelled Bayesian as Baysian

We changed "Baysian" to "Bayesian".

[Q11] Page 11, line 52: typo: left out "for Gs(r)" in the parenthetical expression.

We corrected this.

[Q12] Section 3.5: I'm not sure I understand why you decide to do error propagation the way you decide here. The non-Gaussian distributions in your synthetic example are not surprising, and in fact are to be expected even if the pdfs for Gc and Gs are Gaussian, given it's a non-linear transformation to dlnG and Theta. It seems very unsatisfying to me to use this method that's so powerful and able to handle non-linear and non-Gaussian problems, and then do error propagation by forcing Gaussian distributions on Gc and Gs, and then further assuming Gaussian error propagation. I understand non-Gaussian distributions are more difficult to deal with in terms of finding ways of visualizing the errors on a map, etc., but I think it makes the most sense to propagate the uncertainty correctly at least to obtain the pdfs for dlnG and Theta. At that point, for simplifying visualization, you could calculate a best-fitting Gaussian, or perhaps use the mean and 90% or 95% upper and lower bounds for the parameters, which would likely still be relatively easy to plot.

We agree with the reviewer that propagating the errors by drawing samples from the Gc and Gs PPDFs appears like a powerful method to obtain errors on dlnG and theta. However, after performing a lot of tests, we were very dissatisfied with the results, as explained hereafter, and decided to use the method we had initially proposed instead.

In addition to the synthetic tests we had done for the first version of the paper, we did what the reviewer suggested and propagated the errors on Gc and Gs by drawing random models following their PPDFs and calculating dlnG and theta for each set of Gc and Gs model drawn. This eventually yielded PPDFs for theta and dlnG. However, many of those PPDFs were far from Gaussian, and several had multiple peaks as shown in the example of Fig. S7, which comes from real data inversion and not synthetics. By taking the mean of the resulting theta distribution, we end up with a mean angle that is very far from the mean angle one gets from the mean Gs and Gc (which would give mean dlnG=0.7% and mean theta=60°).

Another way of looking at this is by comparing the anisotropy map of Fig. 11(f) with Fig. S6, which shows the mean theta and its standard deviation at 150km depth as obtained after resampling the Gc and Gs PPDFs. The mean model in Fig S6 is not representative of the mean model displayed in Fig. 11(f) and is thus far from the most likely solution, rendering the discussion of the model and its error bars and comparison with tectonics or other models very difficult.

While we acknowledge the method we chose in the end is not quite as satisfying as getting uncertainties on dlnG and theta directly, we believe it is a better representation of the range of possible models.

[Q13] Page 13, line 41: First reference to figure 10 before figure 9 has been referenced. Figures should likely be re-ordered.

Thank you. We swapped the two figures.

[Q14] Page 14, section 4.2: This is an extremely weak argument with the mean NA model. Clearly, there are minima in the rms curve, and maxima in the vertical gradient curve shown in figure 11 at every single transition point in the spline parameterization (the points where neighboring splines have equal amplitudes). These transitions occur at 75, 125, 175, 225, 275, 350, 425, 500, 600, 700, and 800 km depth, and they precisely match the minima/maxima discussed in the text.

In our previous papers (Yuan and Beghein, EPSL, 2013; Yuan and Beghein, JGR, 2014) we demonstrated that the positions of the minima and maxima in the average model do not depend on the spline parameterization. We had tested different parameterizations with more closely spaced and less closely space spline functions, and showed that the model does not significantly change with the spline functions spacing. Of course, if the spacing is too wide the model becomes vertically smoother and we lose some of the model features. We added a sentence in the manuscript to clarify this point.

Furthermore, they are all fairly similar in amplitude with the exception of the deeper minima and large gradient term at a depth of 75 km. The interpreted change at the top and bottom of the TZ is not convincing in these plots in the mean NA model. Additionally, I'm curious about the SVD model curve. To me, this looks nearly identical to the curve from the YB13SVani model, which is somewhat surprising to me, given the different radial spline parameterization of the new model (which has a clear impact on the curves of the NA model). If this really is the correct curve for the new SVD model, that's a little bit more convincing evidence that the discussed signal at the top and bottom of the TZ is a little more robust in a more traditional inverse model. However, for whatever reason, it is not visible or convincing in the new NA model.

We thank the reviewer for pointing out the issue with Figure 11. We inadvertently plotted the rms and vertical gradient for YB13SVani instead of the new model. This was corrected and solves the issues.

[Q15] Page 15, line 50: You say there is a good match to APM. From the figure caption, it appears you use the NNR model. If you're going to compare to APM, it makes sense to compare to more than one reference frame, (HS3 and NNR are basically end members in terms of the amount of net rotation), and it would be good to quantify the match with APM in 2 or more models (i.e. mean angular misfit or the like). It also might be interesting to compare to recent flow models as a function of depth (e.g. Conrad and Behn, 2010 or Becker et al., 2014).

We do not expect other reference frames to yield a better alignment with the anisotropy since our new models are very similar to YB13SVani, which had

been tested against other APM models in Yuan and Beghein (2013). We added a sentence in the new version of the manuscript to convey this information.

And while we agree that a comparison with flow models would be interesting, it is beyond the scope of this manuscript.

[Q16] Page 16, discussion of figure 17: This figure is extremely unclear, and not very convincing to me. It is very difficult to see a coherent global pattern in any of the panels to me, yet you claim there's no global consistency in 220, but good consistency at the top and bottom of the TZ. I'm not saying there's nothing there, but the figure does not show it clearly. Perhaps you could define a mean normalized angular difference and a standard deviation. A consistent global signature would presumably have a relatively high mean difference and a relatively small stdev, while a more spotty signal would have a smaller mean and larger stdev. It would also be important to compare this statistic across other minima in the rms curve from figure 11, to better make an argument whether the changes observed at the top and bottom are any more significant than the changes that occur between every other set of splines.

We agree with the reviewer that the figure was extremely unclear and decided to remove it. We now display the results in a different way in Figs. 16 and 17. They are discussed in the Results section.

Overall, I would like to see this study published, as quantifying error in tomography is underrepresented in the literature overall, and even more so for anisotropic tomography. This approach is very promising, but there are a few significant issues that need to be resolved. 1) The authors should address the effect of allowing B and H terms as free parameters on the final model and uncertainties. 2) The error propagation should take advantage of the ability of the method to handle non-Gaussian distributions in some fashion, or if the authors feel that the Gaussian propagation is superior, they need to defend that choice more clearly, as the "artifacts" they refer to are really simply evidence of non-Gaussian behavior caused by propagation of errors through a non-linear transformation, and evidence that their first proposed method is really superior, in my opinion. 3) The argument for significant change in anisotropy at the top and bottom of the transition zone in the new NA model is not convincing, although the signal does appear to remain in the new SVD model. Minima in the NA model are clearly a function of radial model parameterization, and there does not appear to me to be a significant difference between the minima at the top and bottom of the TZ and the minima that occur at the other radial spline transition depths, with the exception of the large difference around 75 km.

If the authors address these concerns, I strongly encourage the publication of this study.

Reviewer: 2

Comments to the Author(s)
This study is in general well done and deserve a publication in GJI. However the authors need to be more realistic on the advantages of their approach (model exploration using NA algorithm) versus regularized inversion, which are limited in this context. A number of statements are wrong and must be corrected before publication. The authors also use a very smooth dataset up to degree 8. The NA inversion has a tendency to produce short scale variations compared to a regularized inversion (figure 14, 17). There is no reason to believe that these short scale variations are required by the data.

While it is true that degree 8 is dominant in anisotropic maps, we did not invert the data only up to degree 8. We inverted on a 10 by 10 degree grid and only discuss large-scale features of the model as explicitly written in the manuscript (see section "Phase Velocity Resolution"). We never meant to mislead the reader into thinking that the small-scale features are resolved. This is why we use a method that can provide quantitative model uncertainties.

The comments below need to be answered before publication. This requires a major revision of the paper:

Main comments :

1) The NA algorithm allows to address fully non linear problems. However, the authors linearize their problem using partial derivatives (equation 3). For this particular linear problem, it is not clear that using NA represent a significant improvement compared to a regularized inversion. It is for example wrong to suggest that in this particular study, NA allows to explore the entire model space (page 4 line 41, page 9 line 56, page 17 line 9) without any a priori information (page 9 lines 58-59, page 17 lines 10-11). The authors introduce a strong a priori information (see page 10 lines 25-36) : first they parameterize their model with a limited number of cubic splines which impose a priori a vertically smooth model; second they explore only a limited range of model variation (-0.03 to +0.03) around YB15SVaniSVD. In addition, the authors explore only the part of the null space (probably small) that lies within the a priori constraints (smooth model imposed by cubic splines, small perturbations around YB15SVaniSVD). This limits the estimation of uncertainties, as in a regularized inversion. Their claim that they explore entirely the null space (for example in the conclusion page 17) is wrong and it is also not clear that their uncertainties are more accurate than in a regularized inversion. Whether these a priori choices allow to explore a larger part of the model space compared with a regularized inversion (as claimed page 10 line 14 and in the conclusion) is not clear at all with the information provided in the paper : the authors use a cubic spline parametrization similar to the one used in regularized inversions. There is no quantitative assessment that demonstrates that the range of variation allowed around YB15SVaniSVD is greater than the range of model space in

which the solution is searched for in a regularized inversion. In the conclusion page 17, the authors argue that using NA allow them to search the whole model space, including the null space. This is wrong in this study. Their also claim in the conclusion that they do not need to introduce a strong a priori information which is not clear with the information provided in the paper (see above).

The only advantage of using NA in this context is that NA does not require a gaussian a priori information. Using a linear theory as in this paper, the Tarantola Valette least square solution, gives a result which is identical to the Bayesian inversion and allows to compute the posterior covariance and uncertainties with the only additional constraint that the a priori are gaussian. Although using NA is not wrong, the methodological sections should be rewritten (pages 4, 9, 10, 11, 17) to acknowledge the points raised above.

The reviewer's criticisms are perfectly valid. We realize some of the statements we wrote were too strong. On what was on page 4 line 41 in the original manuscript (Introduction section), we changed the sentence into "they can explore a larger part of the model space" instead. Similarly, what is section 3.3 in the new manuscript now reads as "It allows us to map a larger part of the model space (within selected boundaries)". A similar change was made in the Conclusion. We also clarified in sections 3.3 what we meant by no a priori information, which was not the right way of phrasing this. We agree that the parameterization and selected boundaries of the model space search constitute a form of prior information and implicit regularization. We also agree that if the range within which we search the parameters is very small, it is equivalent to imposing a damping. An advantage of forward modeling, however, is that for a given parameterization and cost function, the null space can be mapped, therefore yielding more accurate model uncertainties. This is now part of section 3.3.

2) I'm wondering if the azimuthal anisotropy maps change if Hc,Hs, Bc, and Bs are neglected ? Why do the authors neglect Cc and Cs. These parameters have a 4theta variation but are associated with the same partial derivative than Bc and Bs. Their influence over the Rayleigh phase velocity is therefore similar to Bs and Bs.

The 2 theta and 4 theta dependence of the phase velocity maps is discussed in section 2.1. The motivation for including B and H in the original manuscript was to not make prior assumptions that could affect the uncertainties on the G model. The tests we performed since then showed this was not a huge issue, as explained above and in Fig. S1. Inverting the 4 theta component of the phase velocity map was and still is beyond the scope of this study. In this new version of the manuscript, we neglected B and H parameters as well as the 4 theta dependence of the phase velocity maps.

3) I suggest to remove figure 8 and the second paragraph in section 3.5, as this approach to estimate errors is not retained by the authors.

The figure was moved to the Supplementary material

4) Assuming a gaussian a priori information and a linear theory, it is possible to compute the a posteriori covariance matrix using a regularized inversion. I suggest to compute the a posteriori uncertainties for YB15SVaniSVD (regularized inversion) using equation 23 in figure 13. This will allow to check whether errors obtained using NA and the least square inversion are consistent.

We followed the reviewer suggestion and determined the posterior model covariance matrix to estimate the model uncertainties based on the singular value decomposition method. The results show that the uncertainties calculated for the regularized inversion are smaller than those obtained from the NA (Section 3.3. and Fig. S3).

5) Page 11, line 57-60, page 12 first paragraph: the statement that "NA favor larger amplitude than the regularized inversion since inverse method tend to damp the model toward the reference value" is not clear me. First, the authors should indicate what is the reference model used in the linearized inversion.

We added a sentence in section 3.1 to specify that the local reference model for the inversion is composed of PREM and CRUST2.0.

Second, from section 3.4, I understand that NA explore variations around YB15SVaniSVD and that YB15SVaniSVD is the results of the linearized inversion. If correct, it is expected that NA gives larger amplitudes just because it starts from the result of the linearized inversion, while the linearize inversion damp toward a reference model which is not given. This has nothing to do with the fact that NA would explore a larger part of the model space.

The reviewer is correct and the results depend also on the size of the model space within which we search. To avoid any further confusion, we removed these sentences.

6) Figure 11-12 : the authors observe 2 % anisotropy above 200 km and 1% below. I recommend to use the same unit (dln(G) in %) in Figures 11 and 14 so that the reader can see where 1% anisotropy is resolved on the maps or not.

The figures have been changed accordingly

Puzzled by figure 14 : the author's data are phase velocity maps whose azimuthal terms are resolved up to degree 8 (4500 km fundamental mode) and 5 (6500 km, higher mode). I see on the maps short scale variations much smaller than 6500 km below 250 km depth and smaller than 4500 km in the uppermost 250 km. Are these short scale variations resolved?

Figure 14 has been removed and replaced by Figs. 16 and 17. Figure 17 shows the difference between the fast axes across the 410- and the 670-discontinuities. We calculated this at all grid cells and, in order to avoid over-interpreting those maps, we also filtered them up to spherical harmonics degree 5, which is the expected lateral resolution at these depths.

They also observe a weak anisotropy around 80, 220, 410 and 660 km. This is potentially an interesting result. However these depths correspond to the discontinuities in PREM.

The effect of these discontinuities on the model has already been investigated in Yuan and Beghein (2013) and Yuan and Beghein (2014) and we showed they were not responsible for the observed changes in anisotropy. We added a sentence about this at the end of section 3.2 and in section 4.2.

The author use Visser's results to assume a priori that trade off with isotropic structure is small. As these regions of weak anisotropy correspond to abrupt changes in isotropic structure, a discussion on the possible trade-offs can not be avoided.

We added a few words in the Data and Results sections to note that trade-offs are never completely inexistent.

7) My personnel feeling is that the authors push the interpretation too far in figure 17. Same comment than in point 6 regarding the scale length of variation observed figure 17 versus the sale length of the data.

As mentioned above, Fig 17 was removed and we modified our interpretation.

other points :
page 3 line 43 : remove ")" after 2006

This was removed.

page 6 line 37-38 : "Fundamental Rayleigh waves are note expected to have any 4 psi dependence". This sentence is wrong. Fundamental Rayleigh wave have a 4psi dependence but the strongest partial derivatives of Rayleigh waves are associated with the L parameter (related to SV velocity) which has a 2psi variation only (see for example Leveque et al., GJI 1998). Using 2psi terms only is reasonable but the justification lines 37-50 could be clarified.

We modified this sentence and added the word “strong”: “Fundamental mode Rayleigh waves typically are not expected to have a strong 4Psi dependence in comparison to the 2Psi terms”

Page 6 line 60 : Hc and Hs do not relate to P velocity but to sqrt(lambda/mu) (therefore equal to P velocity only in a fluid where rigidity is null).

We thank the reviewer for pointing to this. It is now corrected

Page 9 line 28 : "dc1 and dc2 do not depend on Moho depth". This is wrong. If you change the Moho depth, you change the average dispersion along each path which mean that you change the isotropic maps and the anisotropy as well. If this was true their would be no need account for Moho depth on the partial derivatives.

We agree that changing the Moho depth would change the dispersion curve and this is not what we meant to say here. We meant that perturbations in Moho depth do not appear explictly in the equations of Montagner and Nataf (1986) (R1 and R2 terms in their equation 4) and is thus not a variable to invert for from dc1 and dc2. Once measurements are done and an anisotropic phase velocity map is produced, the dc1 and dc2 terms can be used to invert or G (and B and H). We removed the confusing sentence

Figure 7 : there is no panels c and d on the figure 7

Thank you for noticing. The caption was changed to reflect this.

page 13, line 28 : off-diagonals -diagonals

This was corrected.